UC Davis
UC Davis Electronic Theses and Dissertations

Title

Investigating Out-of-Equilibrium Processes in Halide Perovskites with Environmental Scanning Probe Microscopy

Permalink

https://escholarship.org/uc/item/6mf064z7

Author

Deniz, Ece

Publication Date

2024

Peer reviewed|Thesis/dissertation

eScholarship.org Powered by the California Digital Library
University of California

Investigating Out-of-Equilibrium Processes in Halide Perovskites
with Environmental Scanning Probe Microscopy

By

ECE DENIZ
DISSERTATION

Submitted in partial satisfaction of the requirements for the degree of

DOCTOR OF PHILOSOPHY

in

Materials Science and Engineering

in the

OFFICE OF GRADUATE STUDIES

of the

UNIVERSITY OF CALIFORNIA

DAVIS

Approved:

Marina Leite, Chair

Frank Osterloh

Saif Islam

Committee in Charge

2024

ABSTRACT

As global energy demands escalate, the need for technological advancements in alternative energy sources becomes crucial to counter climate change. Hybrid organic-inorganic perovskites (HOIPs) have demonstrated great promise for optoelectronics, owing to their tunable bandgap, cost-effectiveness, and simplicity in fabrication. Despite their rapidly growing efficiency and popularity among the scientific community, they suffer from sensitivity to exposure to different environmental stressors (humidity, temperature, oxygen, light, and bias). To quantify the effects of similar surface treatments on perovskites, nanoscale spatial resolution with scanning probe microscopy (SPM) methods are required. Leveraging the ability to resolve electrical characteristics of grains and grain boundaries with Kelvin probe force microscopy (KPFM), we investigate HOIP material systems, exploring the ion migration and charge trapping in grain boundaries in response to varying humidity conditions, and the effect of treatment with additives on humidity stability. Our results elucidate the transience of surface voltage distribution at various humidity exposure durations, due to a complex interaction between the mobile ions and water and the role of grain boundaries in this process. We see improvement in surface voltage and better resistance to humidity with additive treatment. Understanding the exact mechanism of interaction of water with photovoltaic materials is essential to harness the full potential of these materials for their application in commercial solar technologies. Overall, we anticipate the environmental, *in situ* and *ex situ* microscopy developed in this thesis to be extended for interrogating other halide perovskite families, including Pb-free options.

Acknowledgements

To all my mentors, collaborators, friends, and family, whose support made this thesis possible. First and foremost, I would like to acknowledge my research advisor Prof. Marina S. Leite for her constantly motivating mentorship and feedback. I am grateful that I had the opportunity to spend five years in her research lab, solving exciting cutting-edge research problems. I believe that this experience has taught me important skills in experiment design and presenting results and led me become a better researcher.

I must acknowledge my dissertation committee members Prof. Frank Osterloh and Prof. Saif Islam, for their valuable time supporting my research with their perspectives and ideas.

To past and present fellows in the Leite Lab: Abigail Hering, Declan Kopper, Mansha Dubey, Margaret Duncan, Meghna Srivastava, Peifen Lyu, Dr. Richa Lahoti, and Dr. Tao Gong. Thank you for your friendship, support, intellectual and fun conversations and challenging me with questions that help me become a better researcher, it was a pleasure working with you. You all are brilliant and outstanding researchers. I would like to particularly acknowledge Abby and Mansha for PL measurements, Margaret for helping me with the XPS analysis of the perovskites, and Peifen for e-beam & sputter coating of CdTe samples. And I would also thank researchers outside of Leite Lab: Raphaella Banholzer for her enormous help figuring microscopy challenges and Tristan Deppe for machining sample stage parts.

Next, I would like to thank our collaborators who provided us with excellent state-of-the-art

samples, data, and fruitful discussions. To our collaborators with Molecular Foundry in Lawrence Berkeley National Lab: Dr. Carolin Sutter-Fella, and Dr. Do-Kyoung Lee. To our collaborators in the Correa-Baena Lab at Georgia Institute of Technology: Prof. Juan-Pablo Correa-Baena, Dr.Yu An, Sanggyun Kim, Juanita Hidalgo, Diana LaFollette. Most of this work would not be possible without their contribution.

To the staff members in different instrument facilities: Greg Koppel and Keith Jones from Asylum Research, Oxford Instruments for helping me troubleshoot system issues and improve my understanding of the physics and instrumentation of the AFM. To David Hemer from machine shop for his help with sample holder customization.

I gratefully acknowledge all my financial supporters: the National Science Foundation (NSF) award number #20-13647, Jeffery and Marsha Gibeling Fellowship Award and American Chemical Society Division of Energy and Fuels Student Travel Silver Award.

It is extremely important to me to send a heartfelt acknowledgment to the professors in my alma matter in Sabancı University: Prof. Cleva Ow-Yang (Cleva Hoca), because this endeavor would not have been possible without her limitless guidance and inspiration; and Prof. Mehmet Ali Gülgün (Mali Hoca), and Prof. Melih Papila (Melih Hoca), for igniting my passion for research and guiding me toward this path.

To my incredible friends Abby Hering, Ayça Şenol, Begüm Kasap Darbaz, Gökalp Çetin, Irem Efe, Mansha Dubey, Nalan Çetin, Rüstem Özgür, Su Sarlar, and Umur Darbaz: their

presence, even from a distance, has been a source of strength and encouragement through all the highs and lows.

In the realm of scientific endeavors, where the quest for knowledge is often paved with puzzles and obstacles, although unconventional, I find it essential to extend my gratitude to one of the most capricious characters in my dissertation saga: the AFM. Each day with the AFM presented a new challenge, wrapped in atomic-scale mysteries. Despite its temperamental tendencies, it has, ultimately even though begrudgingly, granted me the gift of data, each pixel a token of the battles fought, and the lessons learned.

Finally, to my parents Sevgi Deniz and Gürkan Deniz: thank you for your belief and unconditional support in me with all my crazy life decisions like being a scientist and moving to a whole different continent. I am profoundly grateful to have you as my family.

Ece Deniz

June 2024

Davis, CA

Table of Contents

Acknowledgements iii

Table of Contents vi

Chapter 1:Introduction to materials for solar cells and functional imaging 1
- 1.1 Hybrid Organic-Inorganic Perovskites: promise and challenges . . . 2
- 1.2 Nanoscale functional imaging: scanning probe microscopy . . . 6
  - 1.2.1 Kelvin probe force microscopy . . . 10
    - 1.2.1.1 Ion migration . . . 14
  - 1.2.2 Photoconductive atomic force microscopy . . . 20

Chapter 2:Research Objectives 24

Chapter 3:Instrumentation for environmental, light-dependent microscopy 26
- 3.1 Kelvin probe force microscopy . . . 27
  - 3.1.1 Overcoming sensitivity of KPFM to environmental effects . . . 29
  - 3.1.2 Probe selection . . . 30
- 3.2 Photoconductive AFM (pcAFM) . . . 30
- 3.3 Probing surface electrical properties *in situ* . . . 31
  - 3.3.1 Illumination control . . . 32
  - 3.3.2 Humidity and temperature control . . . 34
- 3.4 Data analysis and image processing . . . 35

Chapter 4:Moisture-enhanced photovoltage response in $Cs_{1/6}FA_{5/6}PbI_3$ 37
- 4.1 Mapping ion migration . . . 39
- 4.2 Experimental methods . . . 41
- 4.3 Probing perovskite materials' humidity stability . . . 44
- 4.4 Conclusions . . . 64

Chapter 5:Chloride-based additives improve moisture stability of $FAPbI_3$ 66
- 5.1 Stabilizing perovskites . . . 68
  - 5.1.1 Role of $MACl$ additives . . . 69
- 5.2 Experimental methods . . . 71
- 5.3 Probing the effects of $MACl$ on $FAPbI_3$ perovskites . . . 73
- 5.4 Conclusions . . . 83

Chapter 6:Conclusions and Outlook 84

Chapter A: Products of This Research **87**
A.1 Awards and Honors 87
A.2 Publications 87
A.3 Presentations 88

Chapter B: Codes utilized **89**
B.1 Drift correction 89
B.2 Watershed-based segmentation 92

Bibliography **93**

List of Tables

1.1 Selected methods to image photovoltaic materials at the mesoscale, including their functional properties and primary information attained. 8

3.1 Sensitivity, current range, and noise level of the pcAFM channels. 31

4.1 XPS binding energy chart for the species Cs, Pb, I, C, N, and O. Species Binding energy (eV) 65

List of Figures

1.1 National Renewable Energy Laboratory chart for world record cell efficiencies from 2024. . . . 3
1.2 Primary environmental stressors driving instability in halide perovskites. . . . 5
1.3 Schematic of an AFM system. . . . 9
1.4 Schematic of a band diagram showing excitation and different types of recombination. . . . 12
1.5 Schematic of an illuminated-KPFM system. . . . 13
1.6 Examples from the literature on surface voltage imaging of perovskite materials. 14
1.7 Schematic of a photoconductive AFM system. . . . 20
1.8 Examples from the literature on nanoscale current imaging of PV materials. 22

3.1 AFM components. . . . 28
3.2 Illumination system of AFM. . . . 33
3.3 Schematic of critical experimental parts. . . . 35
3.4 Watershed-based segmentation algorithm for statistical analysis. . . . 36

4.1 *In situ* temperature and humidity data on $Cs_{1/6}FA_{5/6}PbI_3$ sample. . . . 44
4.2 Microstructure of $Cs_{1/6}FA_{5/6}PbI_3$ sample. . . . 45
4.3 Continuous sequence of dark and illuminated surface voltage maps. . . . 50
4.4 First five surface voltage maps. . . . 51
4.5 Schematic of energy band diagrams perovskite half devices during photovoltage generation. . . . 52
4.6 Illuminated topography and surface photovoltage scans. . . . 54
4.7 First and last topography scans of the experiment. . . . 55
4.8 Illuminated surface photovoltage scans. . . . 56
4.9 Histograms of surface voltage data. . . . 58
4.10 Line profiles of evolution of surface voltage in grains and grain boundaries. . . . 59
4.11 Evolution of surface voltage with respect to changes in the rH levels. . . . 60
4.12 KPFM scans taken at 5% rH post exposure. . . . 61
4.13 Reversibility of surface photovoltage. . . . 62
4.14 Influence of the environmental tests on the perovskite's surface chemistry. . . . 64

5.1 Temperature and humidity data on $FAPbI_3$ samples. . . . 72
5.2 UV-Visible and photoluminescence (PL) spectra of as-spun samples. . . . 73
5.3 Illumination-dependent KPFM maps. . . . 75
5.4 Statistics of illumination dependent KPFM. . . . 77

5.5 Photoconductive AFM maps. 79
5.6 KPFM maps of pristine and rH exposed $FAPbI_3$ and grain boundary statistics. 81
5.7 Humidity-dependent photoluminescence (PL) characteristics. 83

Chapter 1: Introduction to materials for solar cells and functional imaging

To address the global climate crisis, 196 countries pledged to reduce their carbon emissions in the 2015 United Nations Paris Agreement1 by committing to transition from fossil fuels to renewable energy sources.[1] Renewables contributed to 22% of total electricity generation in the US in 2023, with solar energy representing only 3.9%.[2] To meet the 2030 United Nations (UN) goals and the 2050 US National Renewable Energy (NREL) goals of achieving 80% of US energy needs by renewable sources, this percentage must increase rapidly.[3, 4] For a faster uptake in the use of solar energy technologies, the material candidates should have high power conversion efficiency, high stability, long lifetime for the proposed application conditions, and, ideally, low manufacturing costs. Currently, silicon-based photovoltaic (PV) technologies lead the commercial market, with >90% of the market share. This number is projected to decrease to 45% with the widespread of third-generation PV technologies, primarily due to the promise of perovskite solar cells.[5] For large-scale commercialization and deployment of these third-generation PVs, development beyond the current state-of-the-art technology is required.[6, 7]

1.1 Hybrid Organic-Inorganic Perovskites: promise and challenges

Hybrid organic-inorganic perovskites (HOIPs) are promising candidates for optoelectronic applications due to cost, ease of fabrication, bandgap tunability, and exponentially progressing device performances.[8] HOIPs can be manufactured with low-cost materials and simple techniques, such as solution and roll-to-roll processes. There has been an extraordinary rise in the power conversion efficiency of single-junction HOIPs in the last decade, from 14.1% to 26.1% in 2023, which is rapidly approaching the Shockley-Queisser limit of 33.77%.[9] This demonstrates a high potential for replacing today's Si-based PVs. Perovskite-Si tandem cells have on the other hand, reached values up to 33.9%.[9] Figure 1.1 displays the evolution of the cell efficiency values over the years for three generations of PV materials.[9]

The structure of HOIP follows ABX_3 stoichiometry where A-site is occupied by an organic (methylammonium (MA or $CH_3NH_3^+$), formamidinium (FA or $CH(NH_2)_2^+$)) or inorganic (Cs^+ or Rb^+) cation, B site with a divalent metal (Pb^{+2}, Sn^{+2}) and X site with a halide (Cl^-, Br^- or I^-) anion. Compositional engineering of stoichiometric ratios of the halide anion allows tuning the bandgap, and the A-site cation for structural stability by compressing the lattice, making a wide range of stoichiometric combinations possible.



Figure 1.1: **National Renewable Energy Laboratory chart for world record cell efficiencies from 2024.[9]** Other materials and technologies are presented faded to highlight emerging perovskites.

Methylammonium lead iodide ($CH_3NH_3PbI_3$) or $MAPbI_3$ has been used as a model system for HOIP PV research since its first emergence with a power conversion efficiency of 3.8%

in 2009.[10] Through years of research by many groups, better fabrication processes and conditions have been developed on the material level and cell engineering level.[8, 11, 12, 13] A correlation between high crystallinity and high efficiency has been found using morphological characterization. Many of the process parameters that influence the material's morphology, from the concentration of precursor materials[14] to annealing conditions[15, 16] and additives[17, 18], have been extensively investigated with experimental and theoretical work.[19, 20, 21] The anomalous J-V hysteresis has been examined, and the possible cause is suggested as ion migration.[22, 23, 24, 25] Efforts to reduce ion migration through interface engineering[26, 27] and using different precursors[28] have also been inspected. Despite the fast-moving progress in the field, HOIPs optical, electronic, and structural sensitivity under environmental exposure currently still limits their commercialization.[21, 29, 30]

The environmental stressors, classified as intrinsic (temperature[31, 32], light[33, 34] and bias[35, 36]) and extrinsic (humidity[37, 38] and oxygen[39, 40]), as illustrated in Figure 1.2, can affect the morphology, and eventually initiate degradation, which severely impacts their optical and electronic performances.[41] These stressors can induce phase transition of the photoactive dark perovskite phase into photoinactive yellow phases, and can initiate halide phase segregation or decomposition to various byproducts at various timescales, depending on the composition.[41] For HOIP to be applied to commercial PV devices, they must match the reliability of current Si-based PVs that have a lifetime of 25 years.

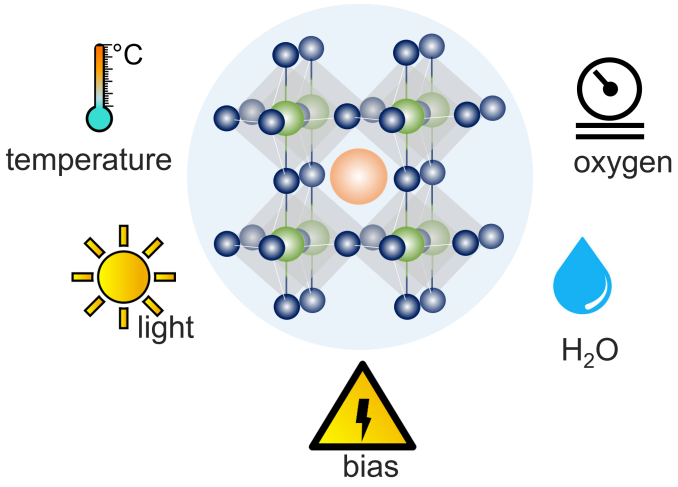


Figure 1.2: **Primary environmental stressors driving instability in halide perovskites.**

In the last decade, substantial progress towards understanding and mitigating the moisture stability challenges of the HOIPs has been accomplished. A record lifetime of 1 year (>10,000h) for a laboratory-scale device has been achieved via 2D/3D interface engineering, where the 2D layer acts as a protective window from moisture.[42] If carefully controlled, moisture is known to impose reversible physical changes on some compositions of HOIP,[38, 43] and moisture treatment during annealing is demonstrated to be advantageous for crystallization and material quality.[44, 45] However, exposing full devices to an elevated relative humidity (rH) for a prolonged time has been shown to enhance halide vacancy concentration, aiding the conversion to a non-perovskite phase and complete degradation into PbI_2.[41, 46, 47] In FA-based perovskites, water functions as a catalyst for degradation, due to their high ionic nature and solubility in polar solvents,[37, 41, 46, 48, 49, 50, 51] but the incorporation of Cs^+ into the A-site has shown to improve the moisture stability of the

perovskite.[47, 52, 53, 54] By tuning the Goldschmidt tolerance factor, crystals with higher stability can be achieved.[12, 54] Optoelectronic devices made of $Cs_xFA_{1-x}PbI_3$ perovskites with a small x to 1-x ratio have demonstrated high efficiency in addition to long-term operational stability.[55] However, further questions regarding how water interacts with the perovskite film and how it can be used to benefit optoelectronic devices are yet to be answered. Nanoscale mapping of the interactions of HOIPs with water is crucial for understanding the mechanisms for material degradation, which is a steppingstone towards establishing them as a reliable technology.

1.2 Nanoscale functional imaging: scanning probe microscopy

Scanning probe microscopy (SPM) is a powerful tool to correlate the morphology of materials with the electrical, optical, and chemical properties resulting from the physical phenomena taking place during interactions with light. Because the HOIP films are commonly heterogeneous, composed of nano- and micro-scale grains, it is ideal to explore the spatial variations in the films with nanoscale imaging.[56] Table 1.1 displays selected scanning probe and other mesoscale methods that are commonly used in PV material investigation by extracting different functional information about the materials through imaging in the dark, under illumination, and/or with applied bias. Imaging methods in column 1 refer to the whole family of techniques under that name, such as KPFM including all Kelvin probe microscopy methods including time resolved KPFM, G-mode KPFM, heterodyne KPFM, etc.[57, 58, 59, 60, 61] SPM offers simultaneous mapping of the morphology and the various other material characteristics such as electrical, mechan-

ical or optical properties, making it a very effective non-destructive tool for evaluating the dynamic surface behavior of HOIPs with spatial resolution <50 nm.[62, 63, 64, 65] Therefore, I have chosen to focus on implementing SPM methods to investigate PV materials.

Recently in HOIP research, scanning tunneling microscopy (STM), which is used to determine and correlate the atomic structures with electronic properties on the materials surface with high lateral resolution (<10 pm), was applied to explore the surface reconstruction at the atomic scale when HOIP materials are exposed to water.[66] Near-field scanning optical microscopy (NSOM) is another SPM technique, which was recently employed to investigate the recombination of photoexcited carriers by spatially resolving photoluminescence (PL) signal.[67]

Atomic Force Microscopy (AFM) is a versatile and popular SPM technique that involves probing morphological, electrical, optical, chemical, magnetic, and mechanical aspects of materials. The primary components of an AFM system are a sharp probe (1-25 nm) that scans the sample surface, a cantilever to which the probe is attached, a laser that is deflected off the cantilever, and a quadrant photodetector to collect the laser signal and record information with a feedback loop to help tracing the surface features accurately, see Figure 1.3. Topography measurements allow for characterization of the grains and grain boundaries and determining the surface roughness. There are many interactions and forces at play when two materials (probe and the sample) are brought to close contact such as electrostatic, capillary, and chemical potential, therefore, there are various AFM techniques that allow imaging electrical, chemical, optical properties of materials in addition to the morphology.[57] Correlating the morphology with electrical methods can give insights into the physical phenomena

	Imaging method	Information
Scanning probe		
	Kelvin probe force microscopy	Work function Band bending Ion migration Charge carrier transport
	Conductive/photoconductive atomic force microscopy (cAFM/pcAFM)	Conductivity mapping Local current distribution Defect localization
	Scanning capacitance microscopy	Doping profiles Carrier concentration Junction depth
	Scanning tunneling microscopy	Electronic states
	Near-field scanning optical microscopy (NSOM)	Photocurrent mapping Local absorption
Other methods		
	Electron Beam Induced Current (EBIC)	Radiative recombination of charge carriers Electrical activity of defects P-n junction characterization Carrier collection efficiency
	Cathodoluminescence (CL) mapping	Recombination sites Quantum efficiency Defect band emission
	Photoluminescence (PL) mapping	Radiative recombination of charge carriers Carrier lifetime Energy band gaps

Table 1.1: Selected methods to image photovoltaic materials at the mesoscale, including their functional properties and primary information attained.

that govern the HOIP film stability and the performance.

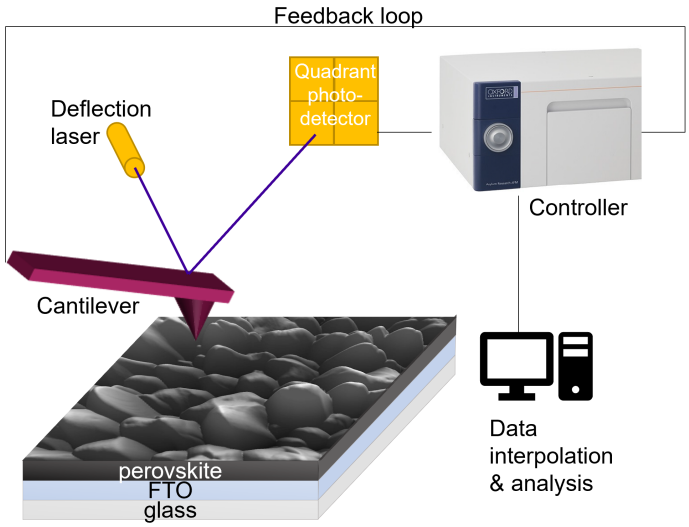


Figure 1.3: **Schematic of an AFM system.** Principal components are shown during a topography scan (not to scale for clarity.) The probe-sample interactions deflect the position of the laser hitting the quadrant photodiode, recording the coordinates.

Probing surface electrical signals in photovoltaic materials via the electrical modes of AFM has been an important diagnostic tool to investigate the spatial variation of local voltage and current with respect to the material's topography.[57, 68] In a controlled environment with varied stressors, these techniques will help identify the surface-level interactions and degradation mechanisms of HOIPs.[69, 70] There are near endless possible compositions in the halide perovskite realm, which all function and respond to the environmental effects in their unique way and pace. These measurements aid in pinpointing the specific mechanisms that drive important events that lead to degradation. Combined with the latest technology, these techniques can provide high-resolution scans down to atomic dimensions at sub-second speeds, providing versatile investigation of functional properties.[71] Furthermore, with the

evolution of automation, machine learning and next-generation artificial intelligence technologies, acquisition and data analysis of scanning probe microscopy have been broadened into new perspectives.[58, 59]

1.2.1 Kelvin probe force microscopy

In this section, we discuss the significance and operating principles of the Kelvin probe force microscopy (KPFM), its application in PV, and mechanisms leading to surface voltage/photovoltage signals. At the macroscopic scale, the Kelvin probe method measures surface voltage based on the difference between the work functions of the sample and the probe through a parallel plate capacitor.[60, 61, 72] It can monitor surface voltage distribution by measuring the contact potential difference (CPD) between a probe tip and the material surface based on the work function difference following:

$$V_{CPD} = \frac{\Phi_{tip} - \Phi_{sample}}{-e} \qquad \text{equation 1}$$

Where Φ is the work function of the sample and the probe, and e is the elementary charge. The work function is energy required to remove an electron. Tracking the changes in the local work function can provide information about the chemical composition, phase change, and electronic properties.[73, 74, 75] The outermost 5 atomic layers contribute to the work function of a surface, which makes KPFM a surface-limited technique.[76] The continuous 3D symmetry in the bulk lattice is broken near a surface, making surface localized states exhibit different work functions than the rest of the sample. The surface

of a material involves many imperfections including point defects, dangling bonds, and impurity atoms adsorbed from exposure to oxygen, humidity, or other contaminants, which alter the localized energy at the surface. Therefore, surface voltage is generated as a result of local variations in the work function, including the accumulation of surface dipole in the space charge region.[60, 72, 77, 78] Illumination-induced changes as a result of the generation and transport of charge carriers, charge redistribution, etc. are referred to as surface photovoltage.

Illumination-induced changes in semiconductors have been analyzed with surface photovoltage (SPV) characterization since the 1940s.[79, 80, 81] For consistency with the literature in the photovoltaics field, SPV is referred to as the change in the signal acquired by subtracting the KPFM data acquired in the dark from the illuminated ones.[82, 83, 84] An SPV value greater than zero originates from redistribution of photogenerated carriers.[85] At temperatures above 0 K, electrons in a semiconductor have some probability of being thermally excited to the conduction band. When the semiconductor is illuminated with energies equal to or higher than the bandgap, the absorbed photons transfer their energy to excite the electrons, an electron-hole pair is generated as a result of an excitation event. The total number of charge carriers at a given time is limited by recombination events. After the light is switched off, the number of photogenerated charge carriers decreases due to recombination events.[60] Figure 1.4 represents the process of excitation and recombination processes in photovoltaic materials. The work function of a photoactive material changes upon illumination, due to the electrostatic potential between the charge carriers resulting in a change in CPD.[60, 86, 87] The sign of the change in CPD provides information about

the direction of carrier transport.[87, 88] Moreover, the depth of the surface space charge region and the extent of surface band bending changes with illumination. All charge carrier generation, recombination, transport, and any changes in the space charge region affect the SPV.[60, 72] Therefore, the magnitude of SPV is correlated with the density of surface trap states.[78] SPV information gathered at distinct illumination conditions follows:

$$\text{SPV}=V_{CPD}^{light} - V_{CPD}^{dark} \qquad \text{equation 2}$$

where V_{CPD}^{light} corresponds to the surface voltage measured under illumination and V_{CPD}^{dark} corresponds to the surface voltage measured under dark.

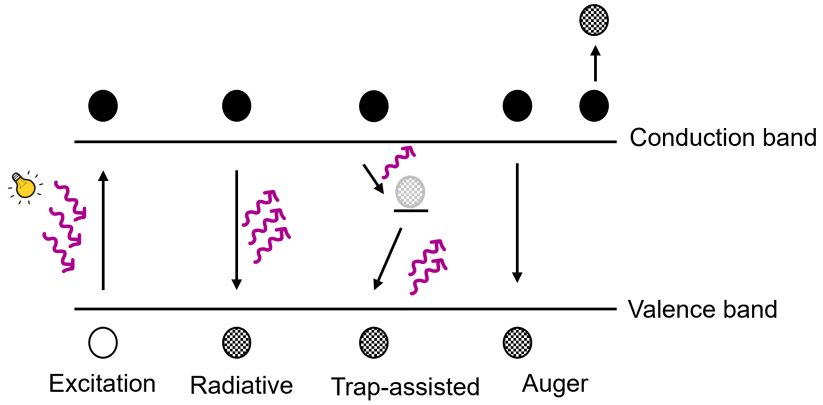


Figure 1.4: **Schematic of a band diagram showing excitation and different types of recombination.** Radiative recombination occurs when an electron and a hole recombine emitting a photon. Trap-assisted or Shockley-Read-Hall recombination is when charge carriers recombine due to the trapping of electrons and holes at the defect states in the band gap. Finally, Auger recombination occurs when the energy given out from a recombination event is transferred to a third carrier to increase its kinetic energy.

We use Kelvin probe force microscopy (KPFM) to map a material's surface voltage with high spatial resolution (<50 nm). KPFM can be utilized to investigate a broad range

of materials, including metals, ferroelectrics, polymers, biological samples, semiconductors including photovoltaic materials, see Figure 1.5 for system illustration and working principle.[82, 89, 90, 91, 92, 93] Recently, KPFM is applied on perovskite photovoltaics to measure the density of trap states at the grain boundaries, which is complementary to measuring carrier recombination lifetime, transport time, and diffusion length, which have been visualized in mixed cation perovskites via transient photo-response AFM, see Figure 1.6a-f. These have revealed variations between trap states and recombination between the grain boundaries of different samples.[94] Moreover, energy band bending under illumination is discovered at grain boundaries, which act as trap states to attract photoinduced charge carriers.[95]

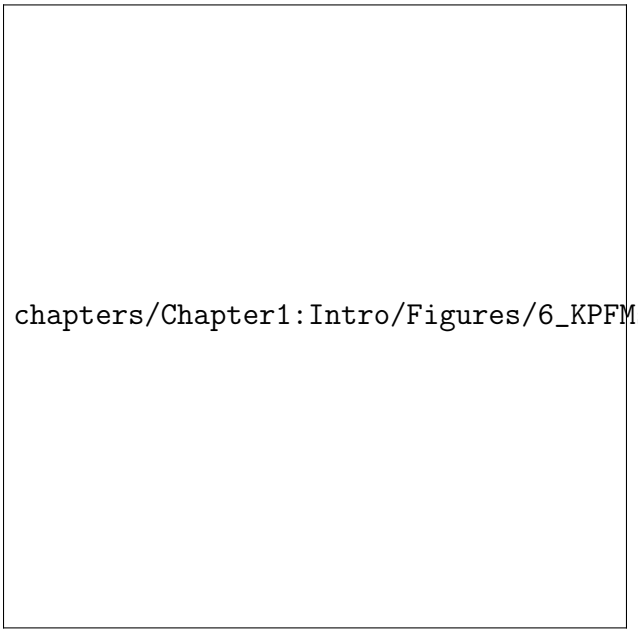


Figure 1.5: **Schematic of an illuminated-KPFM system.** Principal components are shown during a KPFM scan, not to scale. The probe is brought to a specified height with respect to the surface features based on previous topography passes to perform the KPFM measurements. Samples are illuminated from the bottom for photovoltage measurements. See Chapter 3 for more detailed experimental plans and schematics.

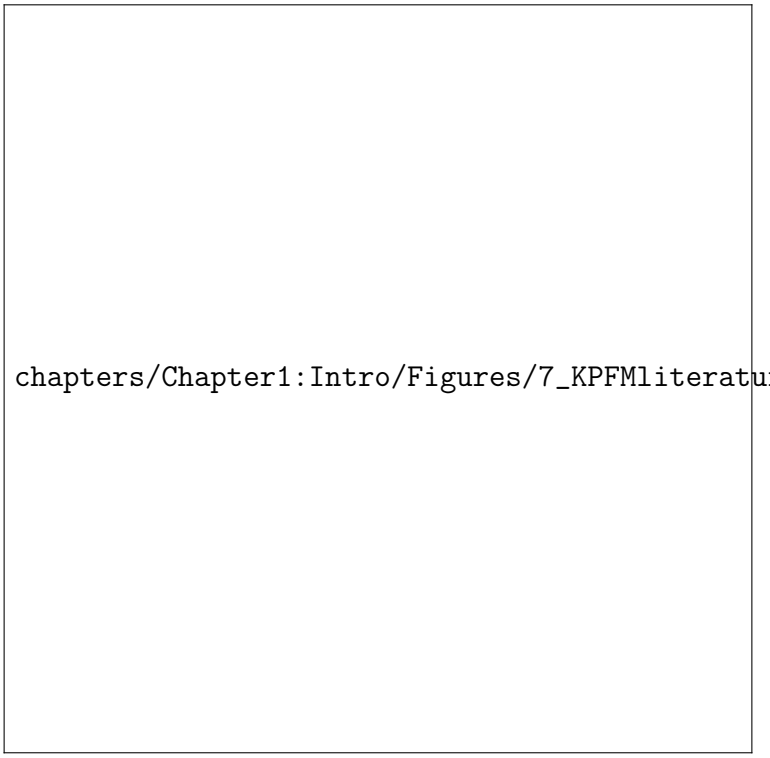


Figure 1.6: **Examples from the literature on surface voltage imaging of perovskite materials.** (a) Topography, (b) surface voltage map, and (c) average in-field loops of a $MAPbI_3$ film.[96] Grain boundaries show enhanced average in-field loops supporting that the Cl^- ions' migration contributes to the hysteresis. (d,e) Charge carrier lifetime, (f,g) charge carrier transport time, (h,i) diffusion length maps across a grain boundary region of $MAPbI_3$ and FAMACs-IBr films respectively, showing FA/MA/Cs-I/Br films exhibiting better charge carrier dynamics than $MAPbI_3$ films.[94] (j-n) Time-dependent ΔV_{oc} maps showing nanoscale distribution of voltage acquired by heterodyne KPFM measurements.[64] (o) Field-assisted ion migration in $MAPbBr_3$ samples mapped with KPFM showing surface voltage evolution after voltage bias is switched on.[71]

1.2.1.1 Ion migration

Although physical processes such as charge carrier motion or local changes in the work function (i.e. due to doping of a semiconductor) have been reported to be the main contributors to the surface voltage, for perovskite materials, a separate unique phenomenon is observed during KPFM measurements, which is the ion migration. [97] Ion migration in

perovskite materials was first reported in halide perovskites by Mizusaki et. al. in 1983.[98] Ion migration in perovskites is an important process to discuss as mobile ions can be responsible for the materials' conduction properties[99], and it leads to many detrimental phenomena such as hysteresis in J-V curves of photovoltaic devices[22, 25, 100, 101, 102], phase segregation[33, 103], and material/device degradation[104, 105]. Conversely, it may have some benefits, such as when ions aggregate near selective contacts, charge transfer can be facilitated and interfaces can be passivated through reducing deep trap levels, reaffirming the complex properties of halide perovskite materials yet to be fully understood.[106, 107, 108]

Physical mechanisms of ion migration in halide perovskites depend on the type of ionic species that make up the A and X site of the ABX_3, composition and morphology dependent on the fabrication methods, and the activation energy for creating defects.[97] Polycrystalline perovskite films fabricated through solution processing tend to have high equilibrium defect density, in the range of $10^{16} - 10^{18} cm^{-3}$.[109, 110] The energy of defect formation depends on the matrix, showing that Schottky defects in a $MAPbI_3$ matrix can have activation energies as low as 0.14 eV, where 0.08 eV for MAI, and 0.22 eV for PbI_3.[111] The mobility of defects also depends on the coordination of the ions in the polyhedra, such as ions at face-sharing coordinates have a lower activation energy for diffusion.[112] The activation energy of vacancy-mediated ion migration of MA^+, Pb^{2+}, and I^- are calculated through first principle calculations for a model $MAPbI_3$ system, and found to be 0.58 eV, 2.31 eV, and 0.84 eV, respectively.[113] The average lifetime of MA^+ is reported as 1.92 s, and I^- as 0.67 ms, (where the photo-generated free carriers have an average lifetime of

2.81 μs). Therefore, halides are the most mobile species at room temperature due to their ionic radii. Because of steric hindrance effects, the ions with a larger ionic radius have been shown to slow down the entire ion migration dynamics, similarly, ions with a smaller ionic radius have been shown to speed up the process.[114] Thus, the activation energy for ion migration will be unique for each composition in mixed cation perovskites due to lattice distortions and require separate investigation (therefore, we do not report specific activation energy and time scales for the compositions in Chapter 4).[115] The photon energy from illumination, thermal energy, chemical potential gradient, and applied external electric field are the main driving forces for ion migration.[116] However, suppression of ion migration is necessary for solar cell applications due to the discussed reasons, for this, composition engineering[52, 117, 118, 119, 120], grain boundary passivation[121], grain size engineering[122] and dimensional engineering[123, 124, 125] have been used to mitigate the effect of mobile ions.

In a part of this Thesis (Chapter 4), we investigate the effect of environmental conditions on ion migration, measured with KPFM. Therefore, it is imperative to explain how this phenomenon is measured through this technique. In a study by Xiao et. al., KPFM measurements are used for a $MAPbI_3$ model system with varying external bias in the dark to help investigate the changing surface potential as a result of ion drift.[116] With negatively charged MA^+, Pb^{2+} vacancies (V'_{MA} and V'_{Pb}) acting as p-type doping by attracting holes, and positively charged I^- vacancy ($V_I^{\bullet}$) acting as n-type doping by attracting electrons, switchable photovoltaics are created through electric field-induced poling.[116, 126, 127] This doping tunes the work function through band bending.[116] Next, migrated ions

accumulating on surfaces and interfaces through illumination, affect the internal electric field, leading to the generation or alteration of space charges.[107, 116] With KPFM we measure the local surface charge distribution, i.e. combination of photo-generated carriers and charges that transfer to the space charge layers to compensate for charge imbalance. Therefore, with careful experimental design, we can detect changes in surface potential as a result of ion migration. The sign of SPV is related to the direction of movement of the charge carriers. In illumination-dependent KPFM measurements, a positive SPV (increase in voltage with light turning on) means that the electrons move away from the surface and holes move towards the surface.[82] Slow decay of potential (or increase if electrons move towards the surface, depending on the order of layers composing a sample) after the light is turned off is a signature of ion migration.[36, 63, 64, 82, 89] Photo-generated carriers and mobile ions have shown to interact and create non-radiative recombination centers in $MAPbI_3$ due to deep traps, however, this is not seen in FA- or CsFA-based chemistries, due to their robustness and better stabilities than the $MAPbI_3$ model system.[36]

KPFM experiments investigating the presence and effects of ion migration are extensively reported in the literature. Band excitation KPFM measurements reveal that slow-moving species, particularly cations, are responsible for the J-V hysteresis observed in double and triple halide perovskite solar cells, as illustrated in Figure 1.6g-i[22, 28, 96] For device-parameter investigations, nanoscale V_{oc} is measured in real-time with heterodyne KPFM by capturing time-dependent changes in local signal due to intragrain ion migration, see 1.6j-n.[64, 128] Moreover, electric field-assisted ion migration and charge accumulation across the layers of a perovskite device have recently been imaged with ultrafast imaging

speeds (<20 μs temporal resolution) via G-Mode KPFM, see Figure 1.6o.[71, 129] Internal electrical potential distribution in PV devices is measured with KPFM, revealing homogeneous electric fields similar to p-i-n type junctions and indicating trapped charges and unbalanced charge transport as potential barriers that can reduce short-circuit current in photovoltaics.[130] Finally, despite the popularity and the increasing number of studies in this field, there is still a huge research gap in understanding the detailed mechanisms of how water interacts with the perovskite material, and the role of different ionic species under varying humidity conditions, influencing the long-term stability of the material, and the interplay between light- and humidity-induced effects and ionic movement within the perovskite structure.

Exposure to humidity is one of the most pressing issues in the field of halide perovskites research, therefore, we chose to use KPFM to interrogate these materials. Kelvin Probe measurements have been previously used for the *in situ* and *ex situ* investigation of the role of humidity.[131] Researchers have investigated the degradation of organic and inorganic perovskites under humid environments to evaluate the long-term stability of champion devices of new chemistries.[73, 78, 132, 133, 134, 135, 136, 137, 138] Humidity is found to increase non-radiative recombination due to an increase in the number of defect centers and dangling bonds at the grain boundaries, thus increasing the trap carriers.[133] Humidity exposure during fabrication leads to grain boundary passivation by suppression of ion migration, which ensures more effective charge transfer through the photoactive perovskite film.[139]

The presence of moisture can further lead to the formation of solvated ions on the surface of the perovskite, such as I^- or MA^+, which can react with photogenerated carriers of opposite charge. In turn, this reaction leads to the formation of neutral iodine atoms, which can be trapped on the material surface, altering the SPV. Additionally, surface ion migration, which is often exacerbated by the presence of water, can result in further amterial instability.[140] Prolonged exposure to water can hydrolyze the perovskite, leading to the formation of PbI_2, which degrades its photovoltaic properties.[140] Therefore, we aim to investigate the photoelectrical properties of the perovskite surface during humidity exposure, prior to any degradation taking place, (we will prove that the experiments are done in this time regime through XPS). An increased number of I^- on the surface, due to the two abovementioned mechanisms, ion migration and solvation, will contribute to a change in the SPV, which can only be distinguished through careful experimental planning. Solvated I^- will increase in concentration as time progresses and the material is further exposed to humidity, until it stabilizes, whether these reactions are facilitated through illumination or not, this should be seen in every KPFM measurement altering SPV only in one direction. Effects of ion migration can only be measured after the light is turned off, and the material evolves towards its equilibrium configuration. The effects of ion migration and the details regarding the experimental setup adopted will be explained in more detail in Chapter 4. Finally, the ion migration of halide ions is proven reversible under light and electric field modulation, controlling the environmental factors can influence ion migration and recovery.[43, 103, 141] These results suggest that similar behavior could be possible if the ion migration is induced by humidity exposure.

1.2.2 Photoconductive atomic force microscopy

Another robust electrical tool that can account for nanoscale inhomogeneities in PV materials is photoconductive AFM (pcAFM). It is used to gather a nanoscale current map of the photoactive film surface, primarily used to map local conductivity variations and resistance.[57, 142, 143] It works by sweeping a conductive tip across the sample surface in contact mode, see Figure 1.7. Charge carriers are collected leading to a current signal. Depending on the type and orientation of the bias, negative bias repels electrons and attracts holes toward the probe.

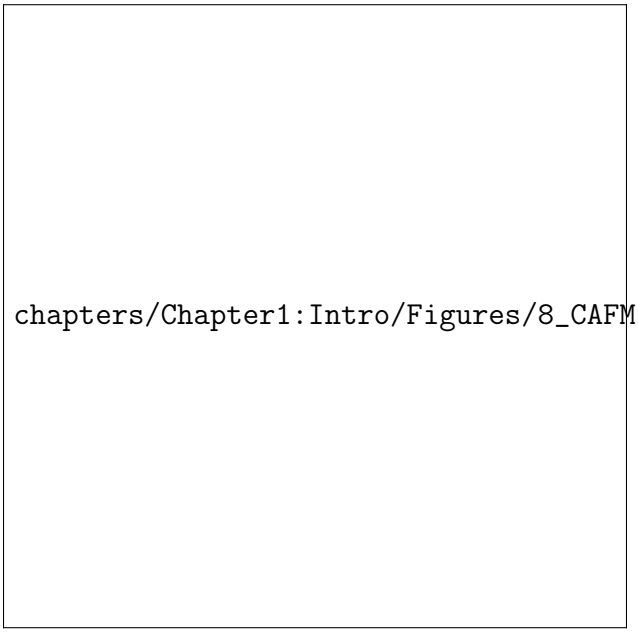


Figure 1.7: **Schematic of a photoconductive AFM system.** Principal components and circuitry of pcAFM, not to scale for clarity. Rsample refers to the internal resistance of the sample. Reproduced from Asylum Research pcAFM resources.

Photoconductive (pcAFM) has been used to map nanoscale photocurrent signal, ion migration, polarization, and photocurrent hysteresis are identified and correlated, recording

enhancement of polarization through illumination, see Figure 1.8a-h.[102] Electronic transport behavior is probed in addition to ion migration and hysteresis, ferroelectric polarization, and correlated with facet orientation, see Figure 1.8m-p.[144] Transport of ions at grains and grain boundaries of polycrystalline HOIP thin films is captured through imaging ion migration originated local current hysteresis, see Figure 1.8q-v.[122] Moreover, individual grains and grain boundaries are observed to be spatially correlated to heterogeneity in short-circuit current.[145]



Figure 1.8: **Examples from the literature on nanoscale current imaging of PV materials.** Photocurrent maps of a triple-cation mixed-halide perovskite film under (a-d) forward and (e-h) backward biases with (i-l) histogram distributions of photocurrent signal in these maps.[102] (m) Topography, (n) short-circuit current, (o) open-circuit voltage maps of $MAPbI_{3-x}Cl_x$ thin films, and (p) efficiency maps derived from the overlay of topography, short-circuit current and open-circuit voltage maps showing the areas of high and low efficiency.[145] (q) Height, (r) amplitude and (s) KPFM image of a $MAPbI_3$ thin film, showing the locations of I-V curves, and I-V curves of (t) high-angle GB, (u,v) low-angle GBs.[122]

pcAFM and KPFM, when used as complementary techniques, are very useful for determining the local electrical phenomena at the nanoscale in many optoelectronic materials. How these techniques are implemented for our research will be explained in more detail in the next chapter.

Chapter 2: Research Objectives

In this thesis, I accomplished the following research objectives related to mapping the nanoscale electrical response of hybrid organic-inorganic perovskites (HOIP) out of equilibrium, upon its exposure to illumination and/or moisture.

(i) Implement environmental, illumination-dependent AFM methods. (Chapter 3) First, I adapted an MFP-3D AFM to interrogate *in situ* the effects of moisture and light excitation on the mesoscale surface photovoltage response of HOIPs. While some features were provided with the commercial tools, others were not, including the optimization of the signals necessary for reliable KPFM and pc-AFM measurements, followed by careful and detailed data analysis.

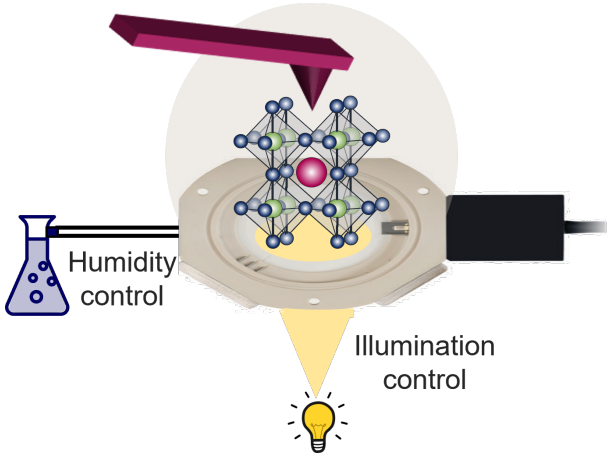
(ii) Nano-image the role of relative humidity (rH) in HOIPs *in situ*. (Chapter 4) Applying Kelvin probe force microscopy (KFPM) over a series of dark and illuminated scans under controlled humidity conditions, I probed $Cs_{1/6}(CH(NH_2)_2)_{5/6}PbI_3$ HOIP thin films at the nanoscale to explain their mechanism of interaction with water prior to degradation. By simultaneously acquiring morphology and surface voltage distribution, I revealed insights on the photovoltage and ion migration dynamics between grains and

grain boundaries at different humidity conditions. Upon initial illumination, voltage rises and stabilizes; and when it is turned OFF, voltage slowly decays with a residual value originating from migrated ionic species. When humidity is introduced, surface photovoltage increases with the level of rH. Our findings illustrate the transient impact of rH on the local electrical behavior on HOIP thin films.

(iii) Resolve the effects of $MACl$ additive on the voltage response and stability of $FAPbI_3$ HOIP. (Chapter 5) Through mapping the materials' surface voltage with KPFM under exposure to high rH for 1 h and 9 h periods, I quantified the influence of $MACl$ on surface photovoltage distribution, enhancing charge carrier transport through passivation of trap states and suppressing non-radiative recombination at grain boundaries, and enhancing photoluminescence. Our findings highlight the significant role of $MACl$ in improving surface photovoltage and promoting moisture stability in HOIP thin films.

Chapter 3: Instrumentation for environmental, light-dependent microscopy

The adaptability of the AFM allows for *in situ* and *ex situ* monitoring of photovoltaic materials under varying environmental conditions. Specific methodological approaches are necessary to get optimized signal from KPFM and c-AFM measurements, followed by careful and detailed data analysis. Therefore, in this chapter, we focus on the experimental configurations and the design choices employed for the environmental AFM measurements presented in this Thesis.



3.1 Kelvin probe force microscopy

I perform the KPFM measurements with an MFP-3D model AFM by Asylum Research (Oxford Instruments), see Figure 3.1a. I utilize the dual-pass method (also referred to as lift-mode) that helps separate the topography and KPFM signals, by first performing a topography line scan, then bringing the probe up to a specified height (100s of nm) from the surface and measuring the CPD with the assistance of a feedback loop. I chose the dual pass is chosen over single pass to minimize crosstalk effects, isolating the electric signal from the topography feedback, at the expense of doubling the scan duration.[146] I chose amplitude-modulated AFM (AM-AFM) over frequency-modulated (FM-AFM) due to increased lateral resolution thanks to the absence of lateral frictional forces.[147, 148] I perform the AC tapping mode topography pass, followed by a lift mode (also referred to as nap mode) voltage sweep. I chose tapping mode to eliminate the contribution of lateral forces to prevent surface modifications and preserve the probe during long-duration experiments, with repulsive mode for higher spatial resolution. I perform the scans with 0.5 Hz scan speed, with 512 x 512 pixels resolution for high accuracy.

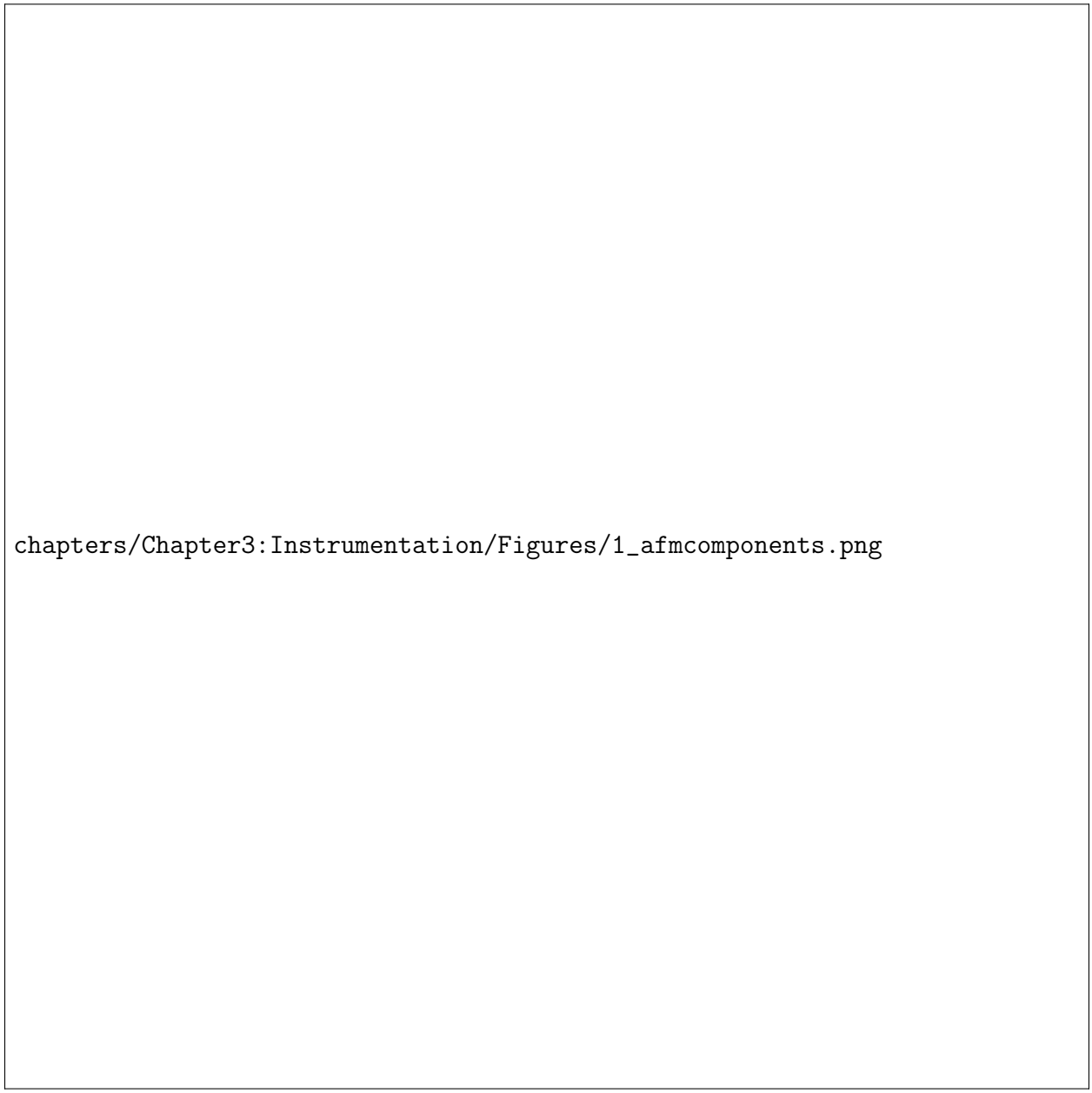


Figure 3.1: **AFM components.** (a) Photograph of AFM setup showing the basic components (head, scanner, base), N_2 tubing, and optical setup. (b) Side view of the humidity enclosure. (c) Humidity enclosure with a sample loaded, electrical contact made on the conductive layer below the photoactive surface, gas inlet, and outlet. The red arrow shows where the probe will align after the AFM head is closed.

I load the samples to the sample chamber in an N_2-filled glovebox and kept in the N_2-purged

sample chamber, see Figure 3.1b-c with <2% rH for 6h prior to scanning to minimize drift and surface water layer. For comparability of different sets of data and reproducibility, I acquire different measurements in the same experiment at the same delta height and voltage amplitude.

3.1.1 Overcoming sensitivity of KPFM to environmental effects

Work function is an extremely sensitive material property that is highly dependent on surface defects and surface chemistry (e.g., adsorbed ions or molecules through oxidation, hydration, or contamination) which is also influenced by the humidity in the environment.[76, 149] Although operation in a vacuum provides surface work function information with the highest precision, KPFM can be accessibly employed for a wide range of experiments in ambient conditions.[150] High humidity levels will not protect from the potential shielding effect from surface water layer, however, qualitative conclusions can be reached if 1) the system is calibrated by allowing the local response to stabilize, and 2) the effect of humidity on the sensitivity of KPFM can be successfully deconvoluted from its effect on the sample.[131, 151] For applications to materials for solar cells, quantitative information can be acquired by focusing on the photovoltage signal instead, which will allow for mitigating the effect of humidity on the sensitivity of KPFM. In this case, I measure the time-resolved photovoltage signal of a humidity-unresponsive SiO2 sample at different humidity levels and stabilization times. Here, I found that leaving the sample in <2% rH environment for 6 h to be adequate to remove the water layer from the materials' surface and to stabilize the KPFM signal.

3.1.2 Probe selection

For the KPFM measurements I used iridium (Ir) coated silicon (Si) probes with 75 kHz of resonance frequency and 2.8 N/m of spring constant. Ir-coated probes are chosen due to their exceptional electrical properties, stability under humidity, and to minimize unwanted catalytic activities. Ir-coated probes are not reported to act as catalysts in chemical processes, thanks to their densely packed structure and high stability, confirmed by the time-resolved measurements. Moreover, Ir metal is insensitive to humidity, and a 6h dry N_2 purge after humidity exposure is adequate to evaporate the nucleated water from the tip of the cone.

While we cannot quantify how the variations in rH affect the Ir tip, we can determine the relative changes in SPV for sets of measurements acquired under the very same rH. Our measurements are relevant because we are comparing the variations in spatial distribution and average SPV values.

3.2 Photoconductive AFM (pcAFM)

I carry out pcAFM measurements with the same instrument as KPFM, with a dual gain Orca holder with two current channels. See Table 3.1 for the range, sensitivity, and noise levels of the two channels. Based on the level of current extracted, it is expected that one of the channels either provides no current, or the current signal saturates. I chose the channels accordingly, providing the best resolution possible. To perform precise pcAFM measurements, I measure the resistances of samples with a multimeter after loading to the

	Sensitivity	Current Range	Typical Noise (1 kHz bandwidth)
Channel 1	1 nA/V	±10 nA	4 pA
Channel 2	1 μA/V	±10 μA	150 pA

Table 3.1: Sensitivity, current range, and noise level of the pcAFM channels.

sample chamber, ensuring a viable contact pathway between the material surface, the metal clip, and the resistor. It is expected to have resistance values in the mesoscale to be an order of magnitude higher than the macroscale measurements, due to a higher number of conductive paths becoming available as the radius of the probe increases. I acquire pcAFM maps simultaneously with topography images, with contact mode. Due to the contact mode, tip wear and surface deconstruction need to be avoided to minimize systematic errors. Thus, I use adequate setpoints and limited the number of scans on the same area until the topography maps start to change beyond the uncertainty of the measurement/instrument.

3.3 Probing surface electrical properties *in situ*

Our main AFM system consists of a modular bottom illumination setup, temperature, and humidity sensors, gas inlets, outlets, and electrical ports, see Figure 3.1a-c. The standard humidity sensing cell from Asylum Research Oxford Instruments has most of the important characteristics for our experiment; a transparent glass slide to mount the sample on, humidity sensor attachment, and gas tubing. However, to control and monitor the environmental stressors *in situ* during the microscopy measurements, we made the following necessary changes to the system: 1) alterations to the sample chamber, 2) built an optical setup to monitor power fluctuations (see Figure 3.2a), and 3) built a setup to control and

vary relative humidity automatically. The standard humidity sensing cell lacked electrical connections, therefore, rectangular parts to hold the metal clips were machined, and attached to the sample holder with silver epoxy, see Figure 3.1c. After the chamber ensured our exact requirements, I mount the sample on the glass slide, and with the AFM scanner head approaching the sample stage from above, the ring ensured a tight seal to keep the sample under 2% humidity unless it was manually controlled. I eliminate possible external illumination sources by covering the enclosure window with black cardboard.

3.3.1 Illumination control

To monitor power fluctuations, I built an external optical setup to split the light beam 90:10, where 10% of the power is detected with a Thorlabs PM100D model digital handheld optical power and energy meter console with a Thorlabs S130C model Si photodiode power sensor attached, and recorded for the duration of the experiment. The rest 90% is collimated to reach the AFM setup to illuminate the sample from the bottom. I illuminate the samples from the bottom to extract the charge carriers more effectively because of their configuration.[152, 153] Figure 3.2b-f shows the light spot illuminating the sample, slightly distorted due to the surface roughness and high optical absorbance characteristics of the PV materials imaged in this dissertation. Here, I use a full spectrum LED, centered at 560 nm for illuminating the sample, see Figure 3.2g. For the duration of the experiments, I control the light manually or automatically. Solar simulator would be necessary for device parameter measurements and efficiency calculations of full devices, however we find illuminating the perovskites with energy above the bandgap using an LED source adequate to induce charge

carrier generation for these sets of experiments, as shown in the KPFM data in following chapters.[154]

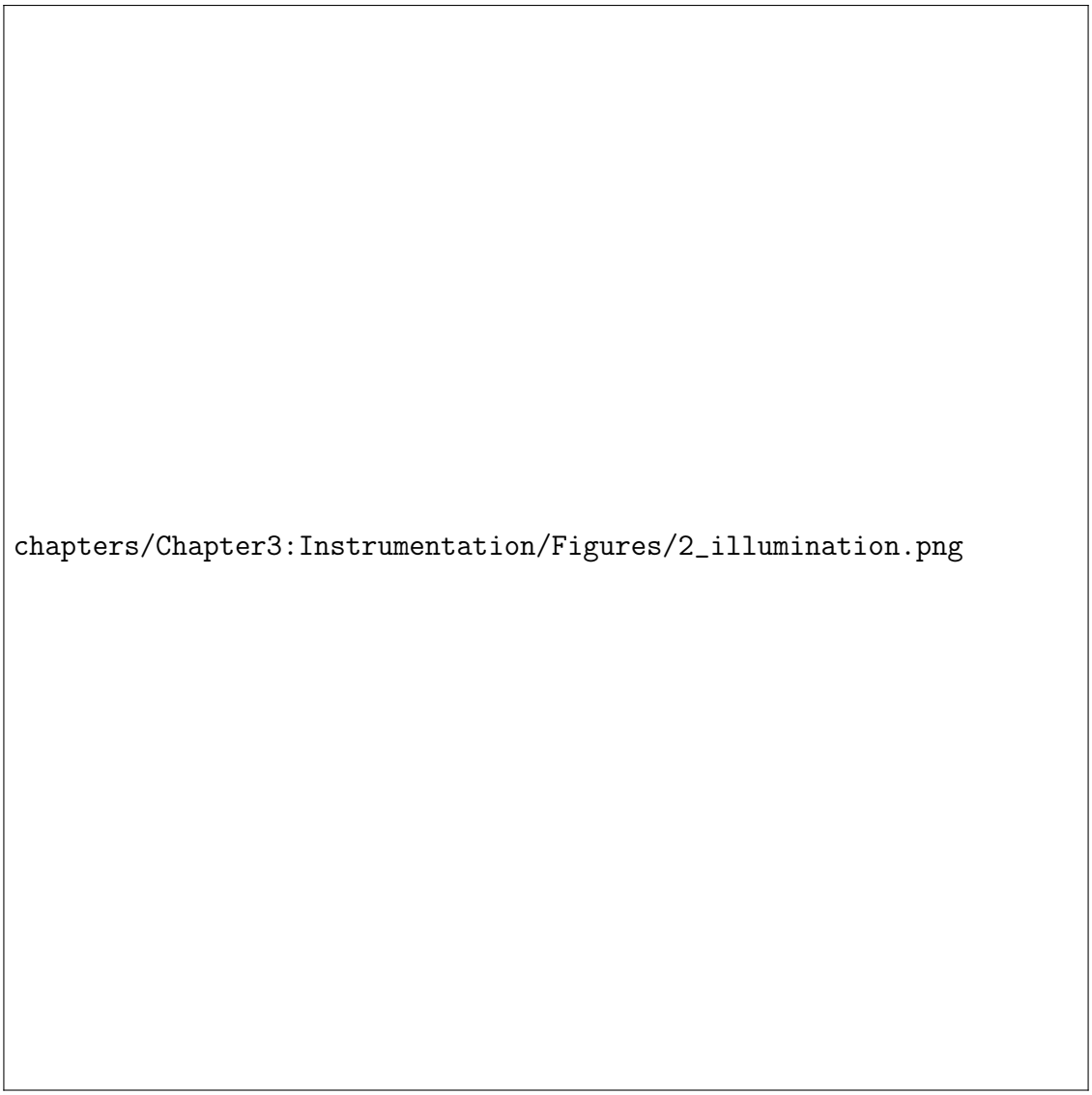


Figure 3.2: **Illumination system of AFM.** (a) The optical setup separates 10% of the LED illumination power for power monitoring. (b-f) Camera image of sample illumination from the bottom, with power density increasing from 0, 20, 50, 80, 100 mW/cm^2 (0, 0.2, 0.5, 0.8, 1 suns), homogeneously illuminating one portion of the sample. (g) Power spectra of the full-spectrum LED used for bottom illumination, also showing a portion of the AM 1.5 Spectrum.[155]

3.3.2 Humidity and temperature control

We built the humidity setup shown in Figure 3.3 to send separate dry and wet N_2 lines to the sample chamber, to control relative humidity (rH). The wet line first passes through a mass flow controller from Bronkhorst then to flowmeters and a water bubbler. The mass flow controller can be programmed for more precise and reproducible control of the rH. This configuration allows automatically bringing the rH to the target value in only 3 to 20 seconds. A Honeywell HIH 4000 humidity sensor measures the rH value inside the sample chamber, which is sealed with a membrane and a metal O-ring, see Figure 3.1b. The built-in temperature sensor in the AFM enclosure records the temperature.

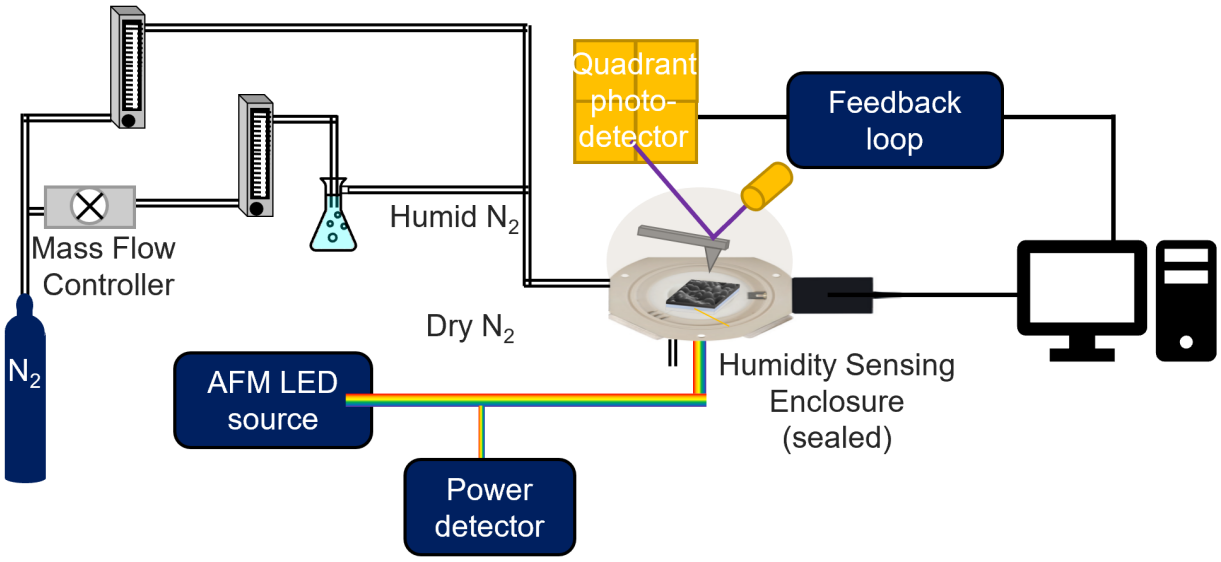


Figure 3.3: **Schematic of critical experimental parts.** The humidity sensing sample enclosure in the AFM system is connected to the illumination system with a power detector that records power data continuously and the humidity setup. The humidity setup consists of a mass flow controller that allows us to precisely control the gas flow with a code. The tubing is then connected to a water bubbler to create a wet line. The dry line is directly connected to the sample chamber from the N_2 tank. The exact inputs required for precise humidity levels measured inside the sample chamber are calibrated prior to the experiment.

3.4 Data analysis and image processing

I wrote a custom Python code to perform drift correction between consecutive AFM maps taken from the same region using a stack registration algorithm (see Appendix B). To perform statistical analysis on grain and grain boundary data, I use a watershed-based segmentation algorithm after automatically preprocessing the data by introducing adequate levels of Gaussian smoothing, gradient, curvature, and barrier level, see Figure 3.4 for the mask applied on topography data following the algorithm.[156, 157, 158, 159, 160, 161] I flatten the topography data with a first-order polynomial fit. Flattening is omitted in voltage and current

data to prevent loss or alteration of information. To achieve photovoltage and photocurrent maps, I subtract dark scans from illuminated ones taken at the same region and conditions following drift correction.

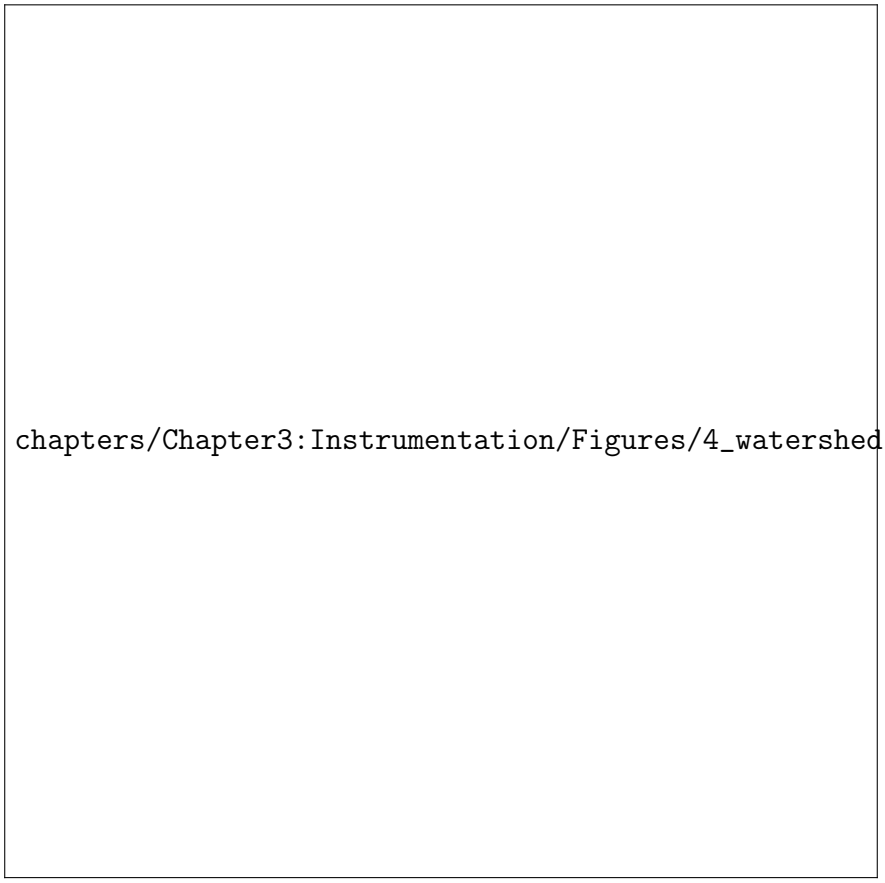
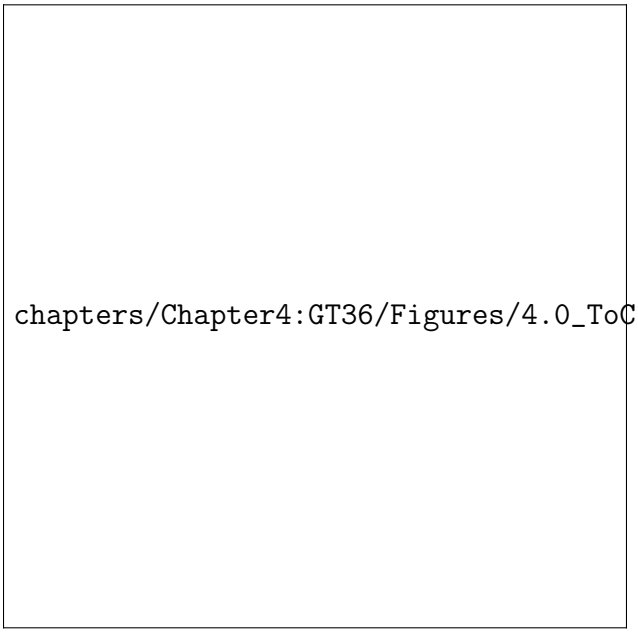


Figure 3.4: **Watershed-based segmentation algorithm for statistical analysis.** a) A sample topography map. b) The same map masked with the Watershed algorithm used to differentiate grains and grain boundaries.

Chapter 4: Moisture-enhanced photovoltage response in $Cs_{1/6}FA_{5/6}PbI_3$

Instability in hybrid organic-inorganic perovskites (HOIPs) upon exposure to moisture currently limits their application in commercial optoelectronic devices. Because these materials are often formed by mesoscale constructs, it is critical to resolve their spatial inhomogeneities, and how they are affected by environmental conditions. Here, we map the spatial variations in surface photovoltage (SPV) at varying levels of relative humidity (rH), deconvoluting the effects of photo-induced and humidity-induced ion migration. Overall, the presence of moisture favors ion motion, significantly more in HOIPs' grain boundaries than in grain interiors. In the absence of water, the surface voltage recovers with 17% (145 mV) excess voltage. Our results elucidate the transient effect of rH on the local surface electrical behavior of this emerging class of optoelectronic material. This chapter is adapted from E. Deniz and R. Lahoti, et. al, Moisture-Enhanced Photovoltage Response in Hybrid Perovskites via *in situ* Microscopy (in preparation).


chapters/Chapter4:GT36/Figures/4.0_ToC.png

4.1 Mapping ion migration

The role of ambient humidity in the degradation of all-inorganic perovskites and hybrid organic-inorganic perovskites (HOIPs) has previously been studied with KPFM ex-situ, showing the initiation of nonperovskite phase formation at the grain boundaries as a result of humidity exposure, and the level of degradation depends on the level of humidity.[73, 132] However, the response of HOIPs to varying levels of rH prior to degradation needs to be clarified *in situ* to deconvolute the effect of ion migration and photovoltage on HOIPs. Ion migration is common in HOIPs due to the softer ionic bonds that are present in halide perovskites, especially where defects and dangling bonds are present, such as grain boundaries and surfaces.[24, 100, 139] Through time dependent KPFM, the anomalous J-V hysteresis is associated with the trapped charges and ion migration.[100, 162] Moreover, due to screening of photovoltage, it will reduce the available carrier-generated current.[139] In most KPFM studies, ion migration is captured by biasing the sample [73, 116, 163], however, illumination-induced ion migration is extensively reported[82, 164], and is measured with KPFM.

To deconvolute the effect of ion migration from charge carriers, we need to consider the lifetimes reported by time-resolved photoluminescence (TRPL, also referred to as PL lifetime) measurements. For hybrid organic-inorganic perovskites, the lifetimes are reported to be in the order of 10-100 ns, where the longest lifetimes are reported to be 20 μs.[165, 166, 167] For the specific composition ($Cs_{1/6}FA_{5/6}PbI_3$, $Cs_{1/6}(CH(NH_2)_2)_{5/6}PbI_3$, or cesium formamidinium lead iodide) that is investigated in this work, the carrier lifetime

is reported to be 191 ns.[55] This time scale being shorter than the bandwidth of our AFM system, it is only possible to see the effect of illumination between two horizontal lines of scan. For optimized structures, the absence of ion migration is reported[82, 139], where the surface voltage stabilizes after charge carriers are generated and reached a concentration. However, on other structures, it is extensively reported that the KPFM signal takes a longer time to stabilize after light is turned on, due to the slow-moving ions.[82]

Ion migration is studied via surface and cross-sectional KPFM to show the accumulation of ionic species at grain boundaries and interfaces, as grain boundaries facilitate the ion migration due to a higher concentration of defect sites and dangling bonds.[122, 129] Garrett et. al. shows that the charge accumulation takes place during illumination, and charge migration takes place after the light is turned OFF until the perovskite material reaches equilibrium, and the residual signal after the light turns OFF helps visualize the phenomena.[63, 64, 82, 89] Therefore, how humidity affects ion migration in real time can only be fully understood via *in situ* measurements in a controlled environment by unraveling the distribution of photo-generated voltage.[56, 64, 83, 89, 122, 129, 168]

Here, we resolve the influence of varying rH on $Cs_{1/6}FA_{5/6}PbI_3$ *in situ* while simultaneously mapping its photo-generated surface voltage with nanoscale spatial resolution. We quantify the dynamic photovoltage behavior of this HOIP as it is exposed continuously to 5, 25, 45, 65, 45, 25, and 5% rH, in a symmetric cycle. Surface voltage changes substantially, where 17% of photovoltage at minimum humidity rises to 70% at the maximum humidity level upon illumination. Quantifying and spatially resolving the distribution

of local electrical properties at the nanoscale enables us to capture an increase in local heterogeneity in the voltage of the HOIP film at elevated rH levels. Significant change in surface voltage in grain boundaries after light is turned off signals higher mobility of ions, however, this does not yet induce material degradation because it reverts with 17% (145 mV) excess voltage at the end of the experiment. Our results elucidate the transient effect of rH on the local surface photo-generated voltage of Cs-FA HOIPs.

Our collaborators in Dr. Correa-Baena's group at Georgia Institute of technology fabricated the samples for this project.[55] We chose to investigate the $Cs_{1/6}FA_{5/6}PbI_3$ composition from the $Cs_xFA_{1-x}PbI_yBr_{1-y}$ family because as a full photovoltaic device it delivered the highest efficiency (12.25%) when compared to 48 additional compositions. Moreover, the corresponding solar cells presented 94% of its initial efficiency when tested under 1 sun illumination for 330 hours.[55]

4.2 Experimental methods

$Cs_{1/6}FA_{5/6}PbI_3$ perovskite (200 nm)/compact + mesoporous TiO_2/FTO/glass samples are fabricated by our collaborators in Dr. Correa-Baena's group as described in reference.[55] First, FTO-coated glass (Kintec) is cleaned with ultrasonication in DI water, acetone and isopropanol. For the electron transport layer a compact TiO_2 (c-TiO_2) is deposited via spray pyrolysis of 480 μL acetylacetone (Sigma-Aldrich) and 720 μL titanium diisopropoxide bis(acetylacetonate) (Sigma-Aldrich) at 450°C, and the substrates are then kept at 450°C for 30 minutes. For the mesoporous TiO_2 (m-TiO_2), the substrate is spin coated with 150

mg/mL diluted TiO_2 paste (Sigma-Aldrich) in anhydrous ethanol for 10 s at 4000 rpm with a ramp rate, followed by sintering at 450°C for 30 minutes. Next, the perovskite layer is spin coated on the substrate by using the precursor solution in a N_2 filled glovebox, from 0.4 M master solutions of CsPbI3 and $FAPbI_3$, which were prepared by dissolving stoichiometric amounts of CsI (Sigma-Aldrich), FAI (Dyenamo), and PbI_2 (TCI America) in DMSO (Acros Organics) in an N_2 glovebox, then pre-heated at 65°C for 1h. The precursor solutions are then used to spin-coat the substrate with a two-step process while using chlorobenzene (CB, Acros Organics) as an antisolvent. The first step involved a 10 sec 500 rpm spin with an acceleration rate of 250 rpm/s, followed by a 70 sec 2000 rpm spin with an acceleration rate of 1000 rpm/s. 5 sec before the end of the second step, 250 μL of CB is slowly dripped. After the spin-coating process, the film is annealed at 65°C for 10 min. The sample is transported to UC Davis with overnight shipping after being sealed in a N_2 filled glovebox, which is a common practice in the halide perovskite field, and kept in a N_2 glovebox until the KPFM experiments.

For the KPFM experiments, the rH is modulated between 5%, 25%, 45%, 65%, 45%, 25% and 5% rH respectively with purging humid N_2, during the experiment. Once illuminated at 5% rH the system reaches a steady state after 30 min, therefore it is enough to complete five illuminated scans, which also matches the relaxation timescale. Therefore, we execute five scans in dark, five scans followed by five scans in dark for each humidity level, and refer to this as 'one illumination cycle'. After we bring the humidity down to 5% and complete the 7th illumination cycle, we refer to this part of the experiment from the start as 'one humidity cycle'. After the humidity cycle, the samples are kept under 5% rH

performing one last illumination cycle scan after 24^{th} hour following the humidity cycle to see any residual surface voltage, see Figure 4.1 for the complete temperature and rH records throughout the experiment. All the scans are performed on the same location on the sample, which is a good representative of the surface texture, and the probe is not lifted up from the surface during the first humidity cycle (105 consecutive scans were acquired in total). The images exhibited little to no thermal drift, however, we employed drift correction for the statistical analyses (see Appendix B). Surface photovoltage is calculated by subtracting the steady-state dark scan from its illuminated scan in the corresponding humidity level. To overcome the surface water barrier due to relative humidity in the sample chamber, a strong setpoint is applied to break through the water barrier, confirmed by the minimal change in the topography signal with increasing humidity.

The XPS measurements were acquired with a Kratos Supra Axis XPS instrument using Al anode $K\alpha$ (1486.6 eV) x-ray sources. Pristine samples are kept under low rH prior to the XPS measurements. All samples were exposed to air for 1 min until pumping down. The base pressure of the chamber was 1.7 x 10^{-8} Torr with 7 mA emission current and a scan size of 450 x 900 μm. The C 1s peak was set to 284.8 eV $\pm$ 0.1 eV to correct for charging effects. ESCApe software was used for the peak fitting of components after performing background subtraction.

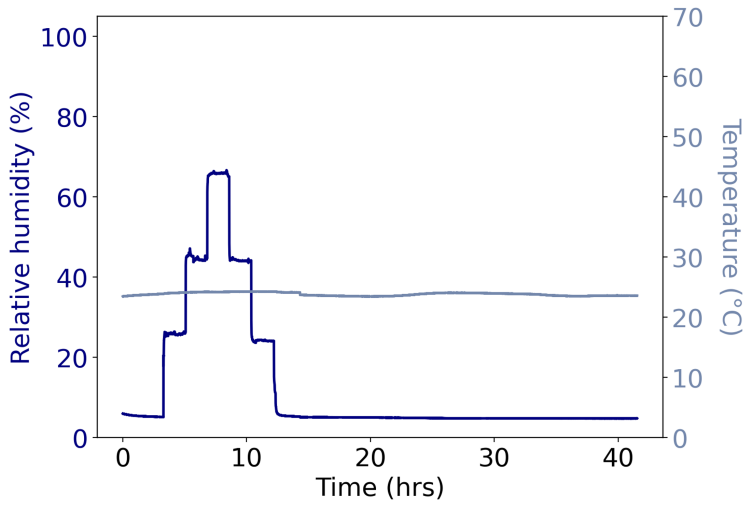


Figure 4.1: ***in situ* temperature and humidity data on $Cs_{1/6}FA_{5/6}PbI_3$ sample.** Measurement of relative humidity (rH) variation and constant temperature for the whole duration of the experiment, as recorded during the AFM scans. The first part of the experiment is completed in 13 h, and post-exposure experiments were conducted 12 h following that. The rH reached the target value ($\pm 1\%$) in 3 to 20 seconds after the first scan of the cycle is started.

4.3 Probing perovskite materials' humidity stability

This halide perovskite composition has been extensively analyzed with x-ray diffraction, photoluminescence, and performance (after being applied to a solar cell device), in another work, therefore we can focus on the microscopy analyses.[55] Scanning electron microscopy (SEM) micrographs in Figure 4.2 show the heterogeneity in grain sizes and distribution of the perovskite thin film, that also agrees with the previous study. Darker grains that are 200-300 nm in diameter correspond to the perovskite domains, and the elongated crystals that appear brighter have a wide range of length, differing from 500 nm to 2 μm, are attributed to $\delta - FAPbI_3$.[55]



Figure 4.2: **Microstructure of $Cs_{1/6}FA_{5/6}PbI_3$ sample.** SEM of $Cs_{1/6}FA_{5/6}PbI_3$ thin film showing (a) uniform film and (b) distribution of grain morphology and size. Images were acquired using a T2 detector, with 10 kV and 1.6 nA.

Figure 4.3 shows a sequence of continuous surface voltage maps acquired in real time to interrogate the $Cs_{1/6}FA_{5/6}PbI_3$ sample under controlled humidity and illumination density

of 100 mW/cm^2. The five initial dark images at 5% rH exhibit a heterogeneous distribution of surface voltage with an average value of -800 mV with respect to the Ir-coated tip, see Figure 4.4 for a larger scale. Grain boundaries show a higher surface voltage than grain interiors. The absence of variation in the signal with time demonstrates our control of ambient conditions during continuous data acquisition. When light is turned ON at the end of frame 5, the average has immediately increased by 10% (80 mV) due to the effective separation of photogenerated carriers, confirming the receptiveness of the perovskite film to illumination. The positive sign of SPV (voltage increase with light turning on) is related to the direction of movement of the charge carriers.[82] Electrons move towards the electron transport layer (compact + mesoporous TiO_2) and the holes move towards the surface, as shown in Figure 4.5a,b.

After the samples reached a steady state after the light was turned ON, the average surface photovoltage rises by 17% (134 mV) and after the light is turned OFF, it stabilizes with a small residual signal of $<$38 mV, for the duration of 30 minutes (close to the duration of 5 complete scans). The contrast between the grain interiors and grain boundaries during light exposure agrees with the literature, where more photo-generated electrons are extracted from grain boundaries than grain interiors and band bending at the boundaries.[83, 89, 168] Although the photovoltaic effect takes place due to charge carriers, where we measure their effect This slow change of signal after light is turned off is attributed to illumination-induced ion migration.[82]


chapters/Chapter4:GT36/Figures/4.4_1_KPFMull.png


chapters/Chapter4:GT36/Figures/4.4_2_KPFMull.png


chapters/Chapter4:GT36/Figures/4.4_3_KPFMull.png



Figure 4.3: **Continuous sequence of dark and illuminated surface voltage maps.** The plots are as a function of rH, varying from 5% to 65%. The white arrow within each image indicates the scan direction. Illumination conditions: full-spectrum LED, 100 mW/cm^2. Each scan takes 7 min 14 sec.



Figure 4.4: **First five surface voltage maps.** (a-e) Consecutive KPFM maps from the initial dark scans, taken under 5% rH.

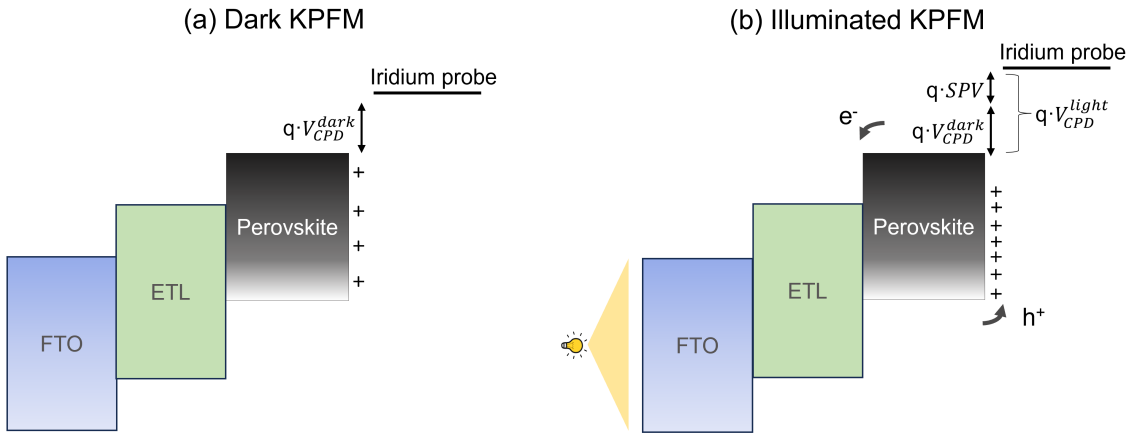


Figure 4.5: **Schematic of energy band diagrams perovskite half devices during photovoltage generation.** Perovskite thin film on electron transport layer (ETL) on fluorine-doped tin oxide (FTO) coated glass substrate in (a) dark, (b) under illumination, when in close proximity with an iridium probe, illustrating the energy bands across different layers. The positive marks depict the space charge region at the surface, which is influenced by the illumination, as the holes that reach the space charge layer influence the depth and surface band bending.

We resolve the effect of rH on the photo-generated voltage response from the last illuminated scans of each humidity step, as presented in Figure 4.6. The topography maps in Figure 4.6a-g indicate that the local electrical response is not accompanied by any changes in the morphology during the duration of exposure. See the first and last topography maps with high resolution in Figure 4.7.

We observe that the surface voltage response of individual grains varies with spatial heterogeneity, and the photovoltage is enhanced by rH.[89] The material's SPV is distributed with local heterogeneity due to the changes in the recombination rates from the inhomogeneous distribution of traps.[55] Leguy, et. al reported for hybrid perovskites

that moisture penetrates through the grain boundaries.[43] Agreeingly, the SPV in grain boundaries is higher than in grain interiors, due to the enrichment of mobile ions at the boundaries, as seen in Figure 4.6k. However, this accumulation is not yet initiating a non-perovskite phase as proposed in Yun, et. al.[73], but it is mostly reversible since the heterogeneity reverted with decreasing humidity as seen from the standard deviations in SPV in Figure 4.6o. The residual signal of 17% (145 mV) shows that the perovskite's photoactivity behavior upon exposure up to 65% rH is only partially reversible for short durations of exposure to rH up to 65%. See Figure 4.8 for the maps in Figure 4.6 represented in separate color scales.



Figure 4.6: **Illuminated topography and surface photovoltage scans.** (a-g) Topography and (h-n) surface photovoltage maps of last illuminated scans at each rH level.



Figure 4.7: **First and last topography scans of the experiment.** (a) First, (b) 105^{th} scan, both taken at dark, at 5% rH conditions.

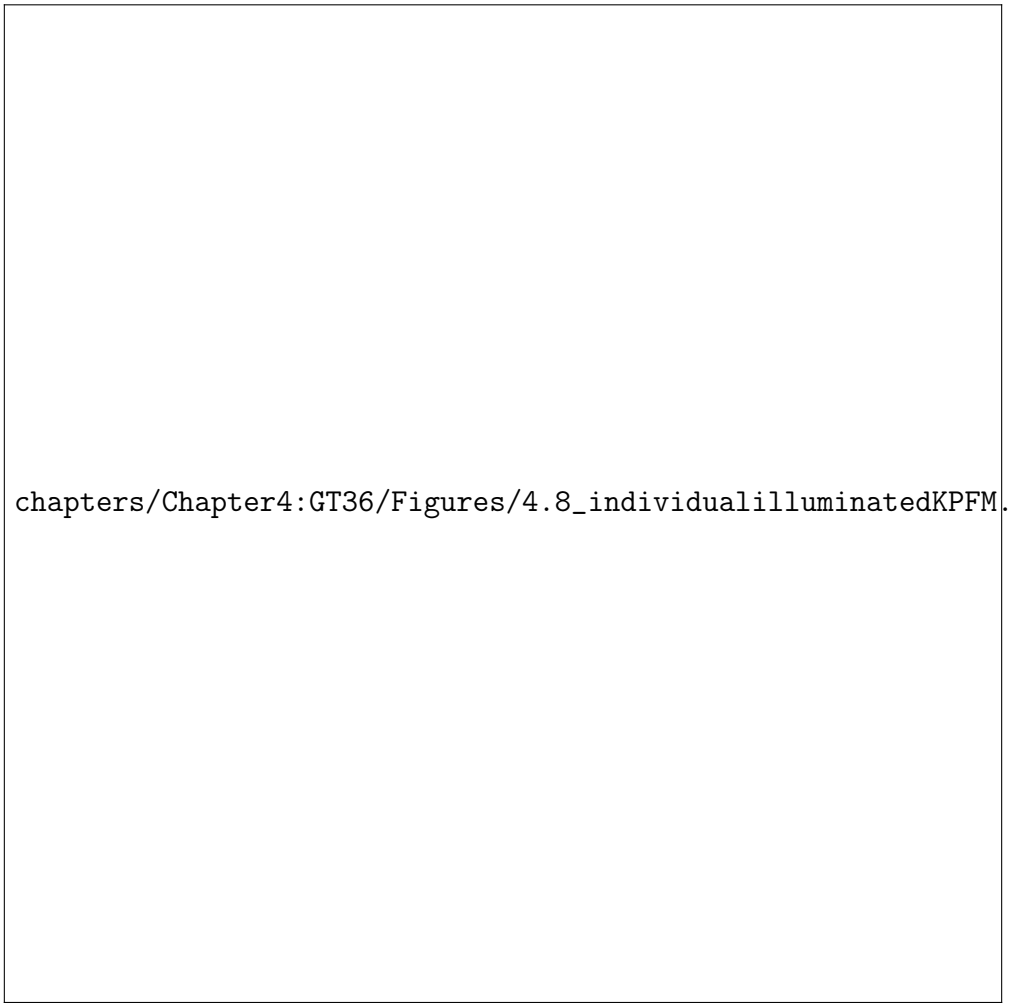


Figure 4.8: **Illuminated surface photovoltage scans.** Surface photovoltage maps of the last illuminated scans at each humidity level, represented in individual color scales to observe changes in homogeneity. Illumination conditions: full-spectrum LED, 100 mW/cm^2.

We gain further insight into the effect of rH exposure on surface voltage by examining how it is distributed at elevated levels of humidity, see Figure 4.9. The unchanged surface voltages in the first five histograms confirm the stability of the perovskite at an almost inert ambient. The light histograms span a wider range during the ramp-up. Combined with increased heterogeneity in the light scans, variation in signal becomes more significant at

these levels, signaling a stronger ion migration taking place. From the voltage difference between boundaries and interiors measured from the line profiles from Figure 4. 10, we notice more vigorous migration of ions at grain boundaries at elevated humidity levels, which aligns with the literature.[83, 122, 129] Visually, the grain boundaries have an overall higher value in photovoltage (see Figure 4.10b). In turn, when the rH is increased, SPV becomes even higher at the grain boundaries when compared to the grain cores. Here, the signal normalization is done by dividing each set of surface photovoltage data by its average. We hypothesize that this spatially dependent behavior is because ion motion is more vigorous at the grain boundaries compared to grain interiors, which results in an enrichment of mobile ions at the boundaries. Upon the completion of a full rH cycle, the perovskite material remains photoactive, including the grain boundaries. The semi-reversible nature of the perovskite's photoactivity behavior persists upon exposure up to 65% rH for the duration of the experiment (9h for rH>5%) tested here.

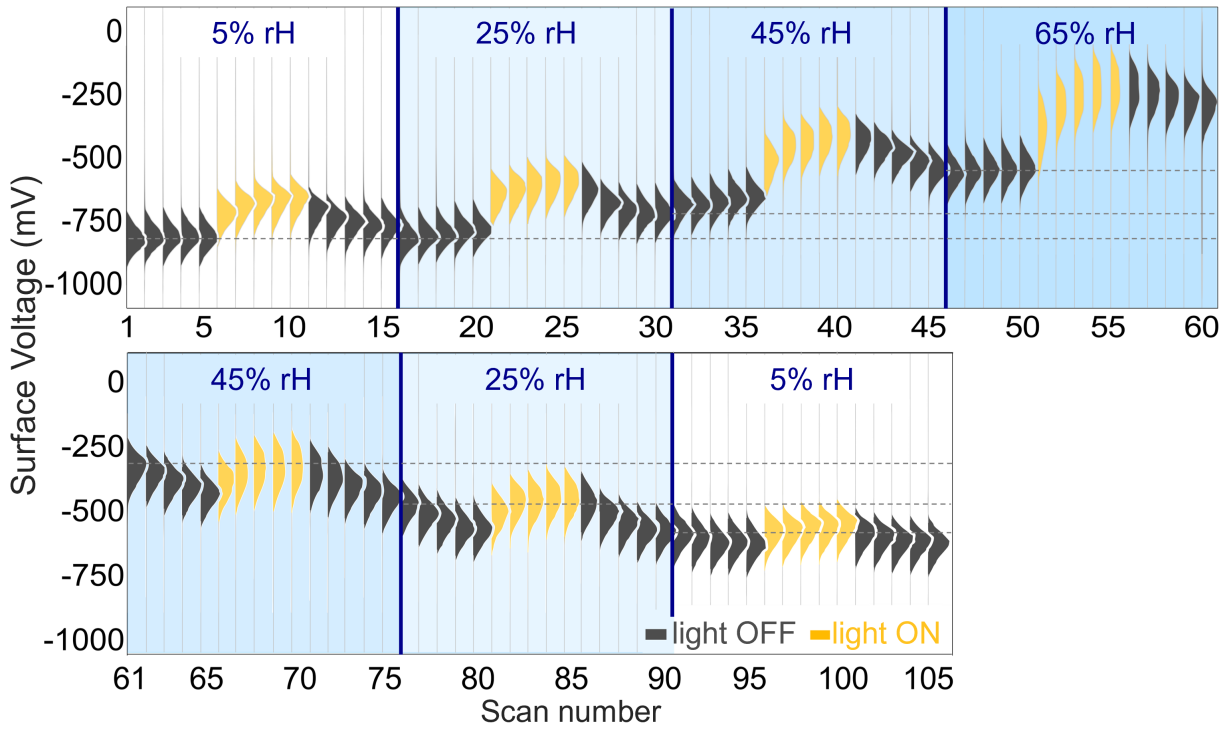


Figure 4.9: **Histograms of surface voltage data.** Represented as a function of scan number, and color coded for light ON (orange) and OFF (grey).

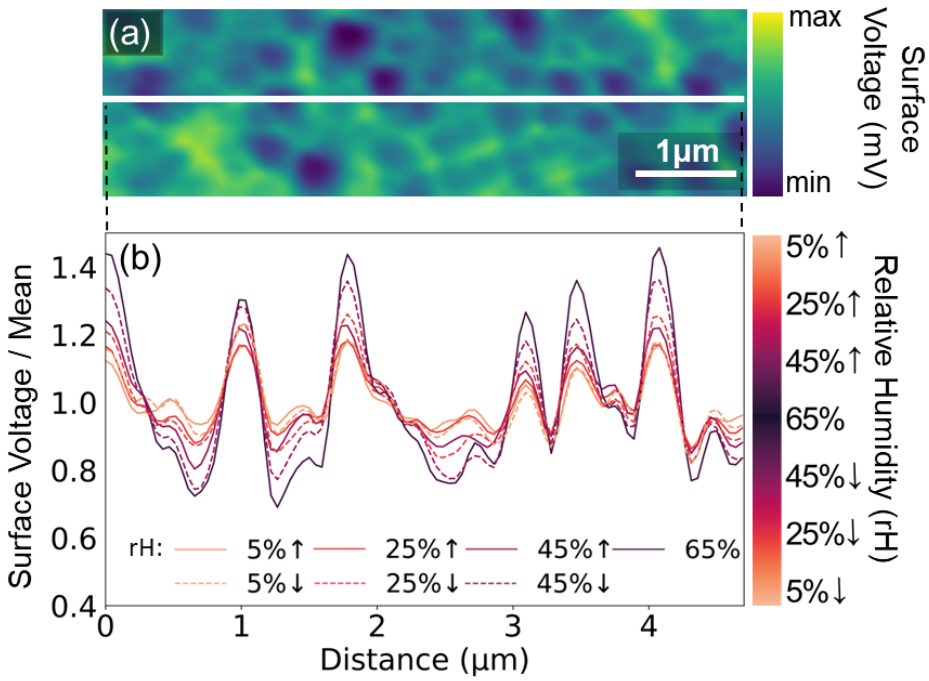


Figure 4.10: **Evolution of surface voltage in grains and grain boundaries.** (a) Surface voltage map from the first illuminated scan (as b shows data from all rH levels, the voltage map is shown only for example), and (b) its corresponding line profile taken at different humidity levels at ramp-up, as described with percentages. The normalized surface voltage is calculated by dividing the data in each line profile by its average.

To deconvolute the humidity-induced variations of surface voltage, we quantify the average values of the maps as a function of changing ambient conditions in Figure 4.11 and observe a reaction in photovoltage to changing humidity, which is shown with red arrows. However, the photo-generated voltage, which corresponds to the rise in illuminated signal from the dark at the associated rH level, rises at 17%, 21%, 28%, and 37% in the ramp up and this tells us that moisture aids the separation of charge carriers. However, it drastically drops afterward, and the photosensitivity is suppressed with further exposure and at the last illumination cycle, as SPV drops to only 62 mV. With post-exposure experiments, we see that it recovered to

122 mV after stabilizing at 5% rH for 24h, see Figure 4.12 and Figure 4.13. This confirms that the suppression of photosensitivity was not permanent.

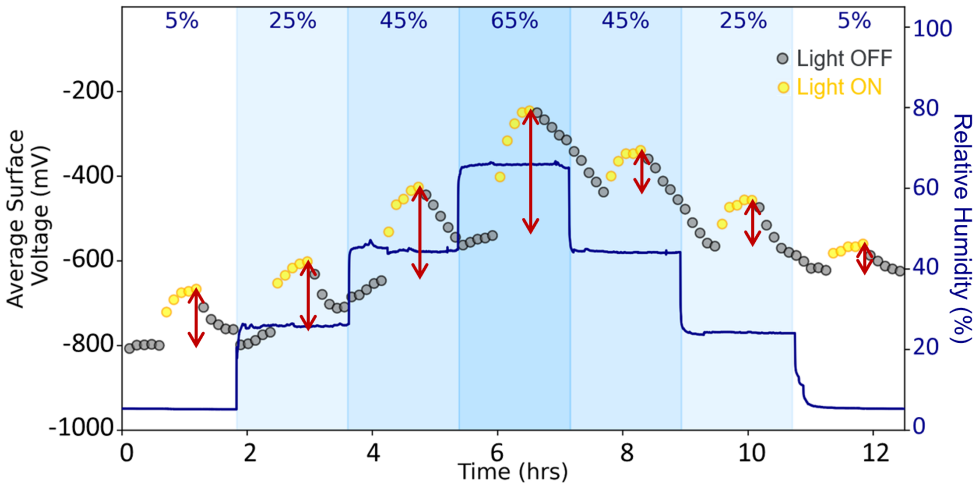


Figure 4.11: **Evolution of surface voltage with respect to changes in the rH levels.** Average surface voltage obtained by calculating the root mean square values of V_{CPD} measured over 6 $\mu^2 m$ areas in each frame, as a function of rH and illumination conditions. The rH reached the target value ($\pm 1\%$) in 3 to 20 seconds after the first scan of the cycle is started.

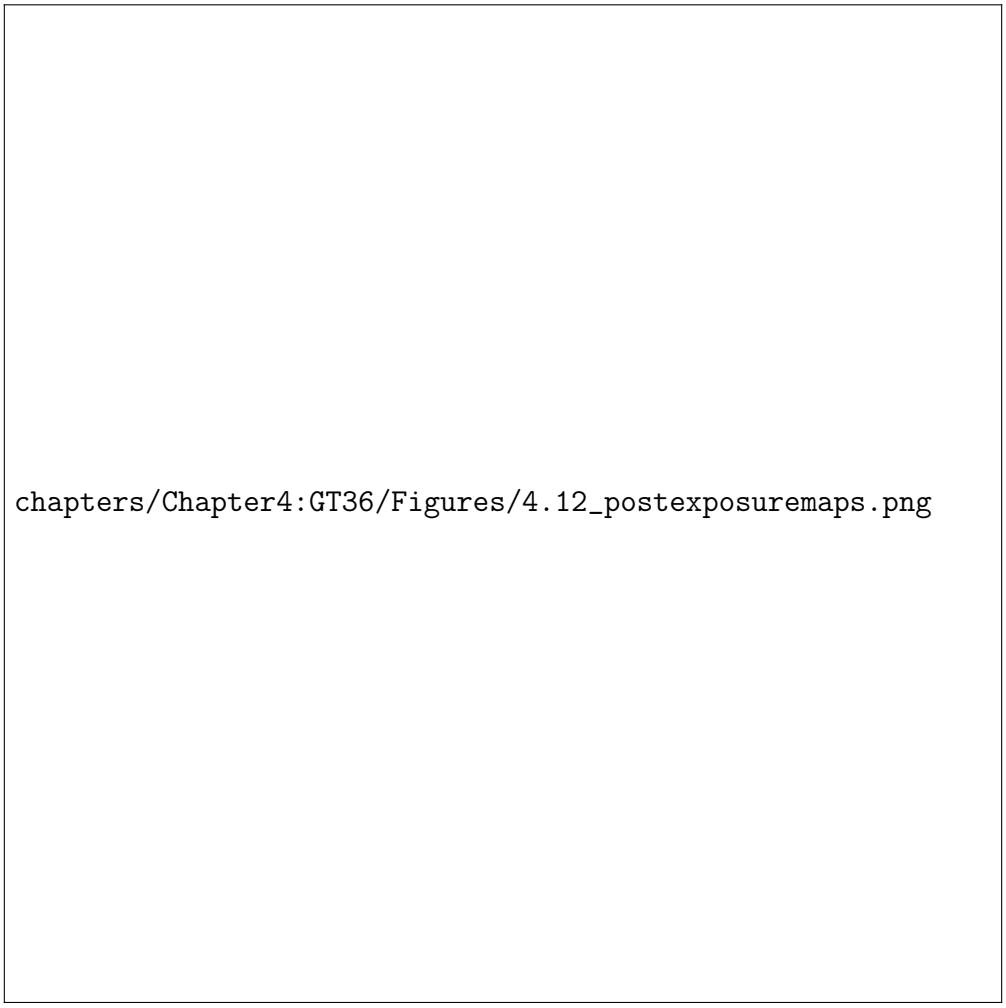


Figure 4.12: **KPFM scans taken at 5% rH post exposure.** Scans taken 24h after the rH experiment. Illumination conditions: full-spectrum LED, 100 mW/cm^2. Each scan takes 7 min 14 sec.

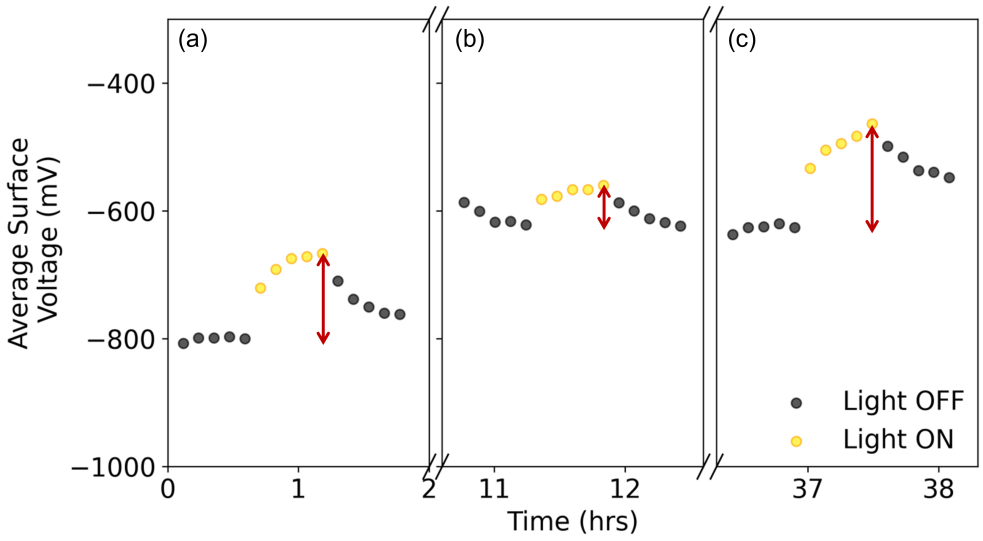


Figure 4.13: **Reversibility of surface photovoltage.** Average surface voltage calculated from 5% rH maps (before humidity cycle, at the end of the humidity cycle, 24h post humidity cycle).

To reveal whether the changes in surface photo-generated voltage signal are due to chemical changes on the surface, we perform X-ray photoelectron spectroscopy (XPS) on the sample before and after the humidity cycle, see Figure 4.14, comparable to the spectra of pristine $Cs_xFA_{1-x}PbI_3$ materials.[169] The ratio of N/Pb^{2+} minimally changed from 6.6 to 6.5, Cs^+/Pb^{2+} changed from 0.29 to 0.3 and there was no shift in the binding energy of the stoichiometric elements in the halide perovskite, these prove that the inorganic and organic cations remain relatively stable during the experiment. However, I^-/Pb^{2+} increases from 1.0 to 1.4 after humidity exposure. A possible explanation is that the unchanged Pb^{2+} content indicates minimal surface reaction, implying that I^- detected on the surface is primarily due to ion migration rather than species dissolution, while Pb^{2+} remains stable within the perovskite structure. However, a second scenario could also be possible considering the I^-

ions being more soluble and reactive. In this second case, the measured difference in voltage would be a combination of migrated I^- and dissolved I^- when exposed to water. The contribution of the oxygen peak at 531.9 eV increases upon humidity exposure, which is typically associated with hydroxyl groups and water molecules stay adsorbed on the surface of the sample after degassing in vacuum.[169, 170, 171] This shows that the voltage gain originated from the interaction of water on the perovskite surface was a combination of chemical and physical changes. See Table 1 for further information regarding the binding energy peak offset values.

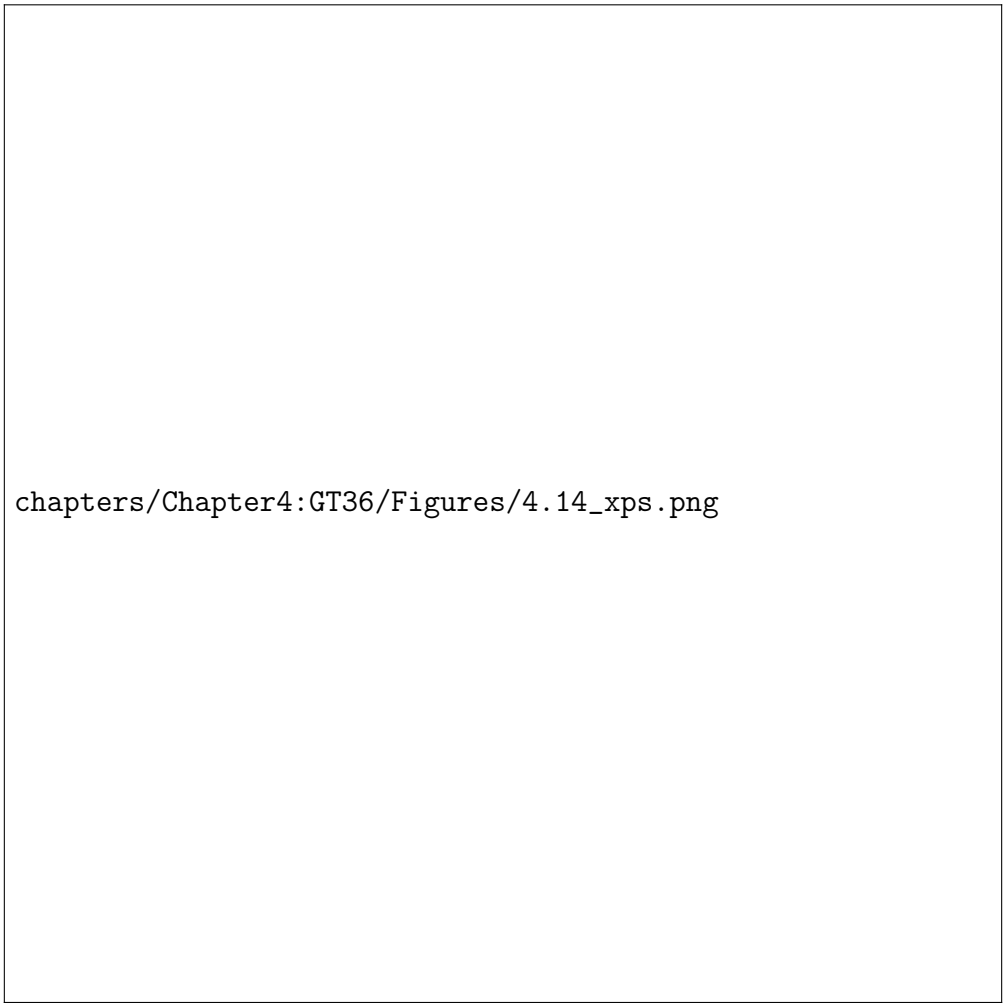


Figure 4.14: **Influence of the environmental tests on the perovskite's surface chemistry.** XPS of Cs 3d, Pb 4f, and I 3d regions of halide perovskite film (a-c) before and (d-f) after the rH treatment. O 1s, N 1s and C 1s regions (d-f) before (j-l) after rH treatment. (m) Survey spectra of species. Data courtesy of Margaret A. Duncan.

4.4 Conclusions

In summary, we resolved, the nanoscale surface photovoltage response of $Cs_{1/6}FA_{5/6}PbI_3$ HOIP upon exposure to light and moisture by performing *in situ*, rH-dependent KPFM

Species	**Binding energy**		
Cs	$3d_{3/2}$ 737.8	$3d_{5/2}$ 724	3d 716.7
Pb	$4f_{5/2}$ 143	$4f_{7/2}$ 138	
I	$3d_{3/2}$ 630	$3d_{5/2}$ 618.5	
C	1s 288	1s 284.6	
N	1s 413	1s 400	
O	1s 531.9	1s 530.7	

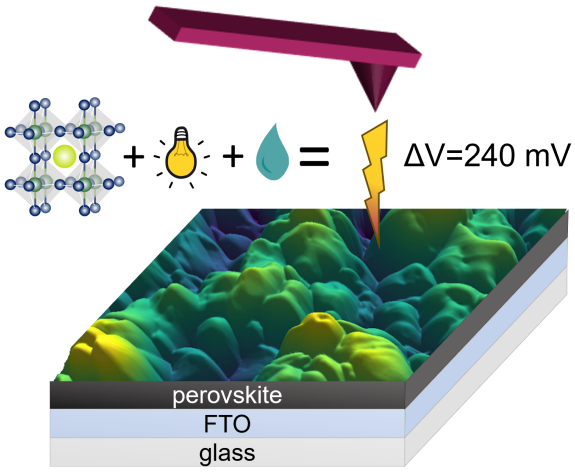
Table 4.1: **XPS binding energy chart for the species Cs, Pb, I, C, N, and O. Species Binding energy (eV)**

measurements. We discovered that the surface voltage is very responsive to varying humidity, as the illuminated response increased by 70% at 65% rH. We found that the $Cs_{1/6}FA_{5/6}PbI_3$ thin film material upon exposure to a cycle with rH levels up to 65%, does not undergo a morphological deterioration, however, the surface voltage distribution evolves rapidly with varying humidity at <10h exposure time. The ion migration at the grain boundaries becomes more significant at the elevated levels of humidity. Moreover, the surface voltage was mostly reverted after the experiment, with recovery with 17% excess voltage. Further *in situ* surface chemical analyses could help deconvolute the effect of surface solvated ions from the internally migrated ions. Understanding the exact mechanism of interaction between the material's surface and water can potentially aid in using this enhanced rate of migration of ions and charge carriers to elucidate the instability of hybrid perovskites.

Chapter 5: Chloride-based additives improve moisture stability of $FAPbI_3$

Halide perovskites present nearly ideal electronic and optical properties for light-absorbing and -emitting devices. However, they suffer from degradation due to environmental stressors such as humidity. One method to mitigate this degradation is the incorporation of CH_3NH_3Cl (methylammonium chloride or $MACl$) in the perovskite films, which can be spatially dependent.. Here, we map the local surface voltage of treated $FAPbI_3$ perovskites through environmental Kelvin probe force microscopy. We find that $MACl$ additive reduces the density of shallow traps at the grain boundaries, besides improving the overall morphology of the grains. The perovskite thin films treated with $MACl$ present a more homogeneous photovoltage distribution signaling improved optoelectronic properties, when compared to untreated $FAPbI_3$. When the films are exposed to 50% of rH, we see $MACl$ aiding trap state passivation and slowing down charge carrier trapping at grain boundaries with increasing humidity. Our findings elucidate the pivotal role of $MACl$ in stabilizing halide perovskites under humid conditions and therefore, a step forward in the understanding of halide perovskite degradation pathways. Further, the environmental scanning probe microscopy platform implemented here could be extended to test the effectiveness of additive agents, including how they enhance the materials' voltage response at the mesoscale. This chapter is adapted from E. Deniz, et. al, Chloride-based additives improve moisture stability

of halide perovskites at the nanoscale (in preparation).



5.1 Stabilizing perovskites

Driven by the prospects of the performance of halide perovskites as photovoltaics, as discussed in Chapter 1, there have been significant efforts to make these materials stable through several strategies. First and foremost, perovskite chemistries are optimized with composition engineering, such as transitioning from MA^+ (methylammonium or $CH_3NH_3^+$) to FA^+ (formamidinium or $CH(NH_2)_2$)-rich cation compositions for longer carrier diffusion lengths and incorporating the smaller cations of Cs^+ or Rb^+ for better stability through compressing the perovskite lattice, or bandgap engineering by adjusting the halide anions.[52, 117, 118, 119, 120] By optimizing annealing conditions, such as the temperature and duration of annealing, and relative humidity during fabrication, the crystallinity of the films can be controlled, which directly affects their optoelectronic properties.[20, 44, 172] Then via interface engineering, passivation layers can be applied at the interfaces that would aid in reducing non-radiative recombination.[117] Engineering the charge transport layers can facilitate efficient charge extraction and reduce non-radiative recombination which could assist in enhancing the overall efficiency. Moreover, hybrid 2D-3D perovskites can be constructed through dimensional engineering, leveraging the stability of 2D and efficiency of 3D perovskites, resulting in higher carrier density and better carrier recombination at interfaces.[123, 124, 125] Finally exploring a wide range of additive-assisted strategies from Lewis acids, bases, ammonium salts, and ionic liquids to lower dimensional perovskites, can help in various ways from crystallization to passivation of defects that arise mainly from processing conditions, to enhancing device stability.[78, 173, 174, 175] In this chapter, we will explore the role of CH_3NH_3Cl (methylammonium chloride or $MACl$) additives in the

nanoscale surface electrical properties and humidity stabilization of hybrid perovskites.

5.1.1 Role of $MACl$ additives

It has been reported in the literature by Zhao and Zhu that $MAPbI_3$ perovskite films with $MACl$ incorporated into the precursor solution, result in solar cell devices with improved performance, from 2 to 12%, thanks to increasing recombination resistance up to two orders of magnitude.[176] Later, Kim, et al. extensively studied the function of $MACl$ additives in a pure $FAPbI_3$ system, and their optimized PV devices have achieved 23.48% of reported efficiency.[177] Overall, $MACl$ is shown to increase grain size and improve the film morphology, where increased grains are advantageous for enhanced charge transport due to fewer grain boundaries which, in turn, are often non-radiative recombination sites.[177, 178, 179, 180] Moreover, $MACl$ modulates crystallization by slowing down the film formation. $MACl$ additives impact the structure lattice by substituting an FA^+ cation with an MA^+ one in the A site, which causes 0.57% shrinkage in the perovskite lattice, thereby supporting the thermal phase stability of α-FAPbI.[52, 172] Conversely, the Cl^- anions are found to be mostly precipitating, following the reaction below with some incorporation into the lattice:

$$FAPbI_3 + \text{y}MACl \rightarrow FA_{1-y}MA_yPbI_{3-x}Clx + \text{(y-x)FACl} + \text{xFAI (y>x)} \qquad \text{equation 3}$$

The precipitates are found to be in comparable concentrations throughout the perovskite thin film, meaning that Cl^- ions were incorporated in the lattice or defect sites

across the film depth.[172]

It has also been discovered that $MACl$ helps with light absorption, carrier transport, defect passivation, and reducing the density of shallow traps at grain boundaries leading to a significant increase in photoluminescence (PL) intensity.[176, 177, 180, 181, 182] Moreover, a more homogeneous distribution of PL signal over the investigated area is reported, dependent on the $MACl$ amount.[182, 183] As a result, increased carrier lifetime and efficiency have been observed in perovskites that have been treated with $MACl$, minimally affecting the bandgap energy.[177]

In addition to improving the optoelectronic properties and performance, $MACl$ enhances the stability of films due to tuning of the tolerance factor and passivation of defects.[177] Several mechanisms are discussed throughout the literature; 1) Cl^- increases the activation energy of phase change that slows down the degradation of $MAPbI_3$ in the presence of moisture, 2) Cl^- helps with passivation of defect trap states, 3) Cl^- aids the crystallization process, 4) Cl^- improves charge carrier lifetime through control of grain boundary structures.[165, 180, 183, 184, 185, 186, 187] Grain boundaries and the surface of the perovskite films have recently been shown to be the most susceptible regions for water and oxygen to interact, due to the high concentration of defects. The addition of quaternary ammonium halides during perovskite fabrication has been shown to minimize water and oxygen permeation through the defects.[188] This result brings up the question of whether a similar mechanism can be found with the addition of $MACl$ additives, which come with many advantages as discussed above, and whether the incorporation of $MACl$ could

provide any benefits towards material stability upon its exposure to humidity. Therefore, this chapter discusses the role of methylammonium chloride ($MACl$) additives on the local surface electrical properties and stability of halide perovskites. Here, we image the surface photovoltage of $FAPbI_3$ thin films with and without $MACl$ additives to spatially resolve its effects at nanoscale using a combination of *ex situ* microscopy.

5.2 Experimental methods

The samples were fabricated by our collaborators in Dr. Sutter-Fella's group from Molecular Foundry at the Lawrence Berkeley National Laboratory (LBNL).[172] The $FAPbI_3$ perovskite thin film is prepared in an N_2 glovebox from $FAPbI_3$ solution, which is made by mixing stoichiometric amounts of PbI_2 (461 mg) (purchased from TCI) and FAI (172 mg)(purchased from Greatcell Solar), with 1 mol of N-methyl-2-Pyrrolidone in 500 μL of N,N-dimethylformamide (DMF, anhydrous). For the $MACl$-treated sample, 40 mol% $MACl$ (27 mg) with respect to the $FAPbI_3$ perovskite solution, is added. The precursor solutions are then used to spin-coat the fluorine tin oxide (FTO) coated glass substrate. The samples are then annealed at 150°C for 30 min on a hot plate. The samples haven't been removed from the glovebox until transport in a N_2 filled sealed chamber, that took <5h. UV-Visible and PL spectroscopy measurements are taken prior to transport, followed by PL, topography, and KPFM measurements taken after transport.

KPFM measurements performed on the perovskite layer followed a similar methodology as described in Chapter 4, using the iridium coated probe. The rH is then modulated

following the rH cycle in Figure 5.1, and ex-situ KPFM measurements are taken at the points labeled as b, d, and f.

Photoconductive AFM measurements are taken using a $PtIr_5$ coated Si probe (PPP-CONTPt, Nanosensors), with 25 nm tip diameter and 0.2 N/m force constant. The illumination follows the same pathway with the KPFM measurements. The contact is made on the FTO layer, and a 2.2 $k\Omega$ resistor is used.

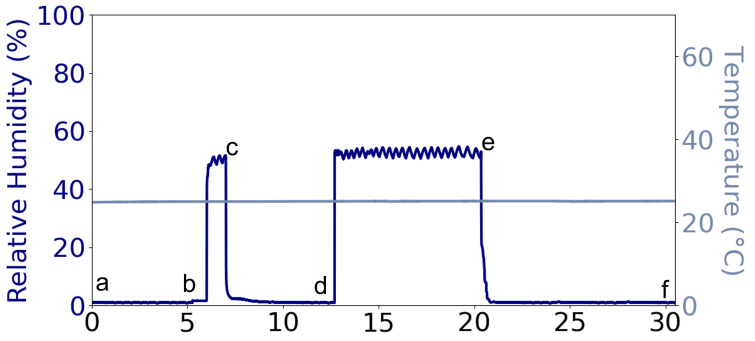


Figure 5.1: **Temperature and humidity data on $FAPbI_3$ samples.** The change of rH and ambient temperature for the whole duration of the KPFM experiment is recorded *in situ*. Points labeled with a, b, c, d, e, and f are time stamps that are labeled for future reference, and KPFM measurements are acquired *ex situ*, after waiting under low humidity for 6h, at time stamps labeled with b, d, and f. Samples at d and f are later referred to as after 1h and 9h of humidity exposure consecutively.

PL spectroscopy measurements are performed on a custom-built PL sample chamber, mounted on an automated translation stage, illuminating one sample at a time by the excitation laser. The relative humidity is controlled the same way as the AFM humidity setup, through purging dry and wet N_2 into the PL sample chamber, with a humidity sensor and a temperature sensor mounted inside of the sample chamber, to track the conditions in situ. The illumination laser has a wavelength of 532 nm, and a power of 1 mW throughout the

experiment. Data is collected by the spectrometer every five minutes for 30 hours.

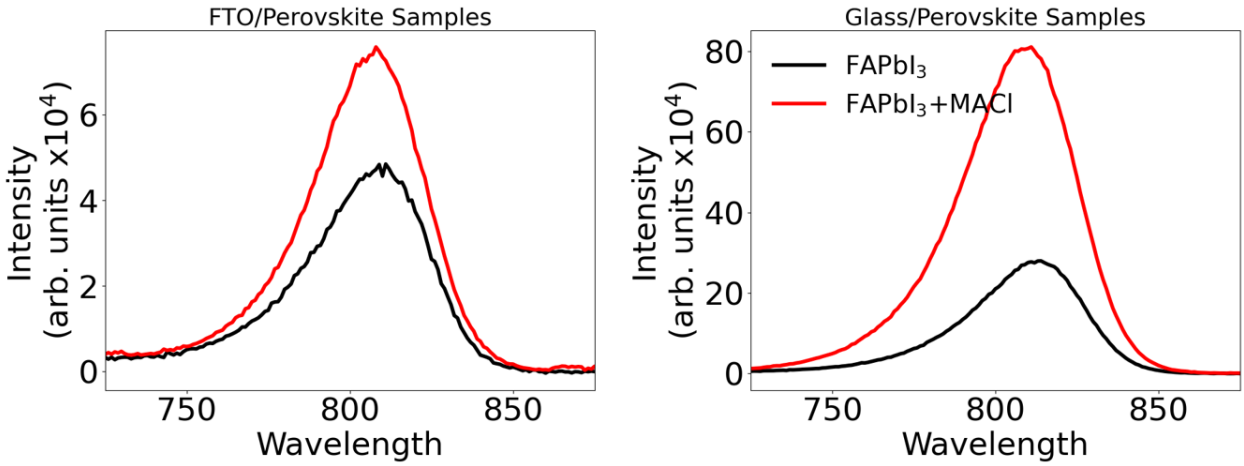


Figure 5.2: **UV-Visible and photoluminescence (PL) spectra of as-spun samples.** (a) PL spectra of $FAPbI_3$ and $MACl$-treated $FAPbI_3$ samples spun on FTO, and (b) on glass. Data courtesy of Dr. Do-Kyoung Lee.

5.3 Probing the effects of $MACl$ on $FAPbI_3$ perovskites

Initial PL measurements in Figure 5.2a,b on as-spun samples show a significant increase in PL yield with $MACl$ treatment, up to 4x increment on the glass substrate. This increment is attributed to $MACl$ treatment helping with improving the crystal quality. A slight blue-shift with the $MACl$ addition in the bandgap is attributed to the MA^+ or Cl^- ion substitution.[177, 189, 190]

Figure 5.3a,d displays topography maps of $FAPbI_3$ and $MACl$-treated $FAPbI_3$ thin films acquired under dark conditions and under illumination (equivalent to 100 mW/cm^2), revealing a more narrow size distribution of grains with $MACl$ treatment. The grains of $FAPbI_3$ sample appear smaller, with an average diameter of 254±45 nm, with domains

of coalesced non-round morphologies. $MACl$-treated $FAPbI_3$ on the other hand, has an average diameter of 406±52 nm. The grain sizes agree with previous recordings of $FAPbI_3$ and $MACl$-treated $FAPbI_3$ in the literature.[177, 178, 179]



Figure 5.3: **Illumination-dependent KPFM maps.** (a,d) topography, (b,e) dark KPFM, and (c,f) illuminated KPFM maps of $FAPbI_3$ and $MACl$-treated $FAPbI_3$ samples consecutively. Yellow circles show the domains with a different voltage characteristic. Illuminated KPFM maps are taken with 100 mW/cm^2 white LED light illuminating from the bottom.

A more homogeneous and uniform distribution of surface voltage is seen in the maps acquired under dark conditions (see Figure 5.3b,e), where the standard deviation drops from

46.1 mV to 13.2 mV. This is reported in the literature as a critical indicator of material quality.[191] Upon illumination, the negative sign of the surface photovoltage indicates that an internal electric field drives the holes toward the FTO, and electrons towards the surface, causing an accumulation of negative charges at the surface. (Mind that this is different than the direction in Chapter 4, as this sample is directly deposited on FTO, without an electron transport layer) In turn, this process leads to a downward band bending, hence the surface voltage signal decreases with illumination in Figure 5.3c,f.

Local changes in the signal with illumination also help identify the two distinct voltage domains in the $FAPbI_3$ untreated sample in Figure 5.3c, with different recombination dynamics, hence resulting in different voltage responses to illumination. $MACl$-treated $FAPbI_3$ sample, on the other hand, shows higher homogeneity in surface voltage distribution in Figure 5.3f, without any domains. The surface voltage of the untreated $FAPbI_3$ sample in the histograms in Figure 5.4a has two wide Gaussian peaks centered at -296 mV is reduced to -425 mV with illumination, and the other one is reduced from -232 mV to -383 mV. The $MACl$-treated sample, however, has a much narrower range of surface voltage, where the peak center reduced from -228 mV to -270 mV. The y-span of the line profiles in Figure 5.4c,d confirms the voltage distribution gained homogeneity with the addition of $MACl$.



Figure 5.4: **Statistics of illumination dependent KPFM.** Histograms of surface voltage distribution in (a) $FAPbI_3$, and (b) $MACl$ treated $FAPbI_3$ samples.

To understand how $MACl$ affects local nanoscale current, we performed cAFM measurements in Figure 5.5. Figure 5.5b,d shows that current is only extracted from grain interiors due to high defect density in grain boundaries, with negative bias that repels electrons and

attracts the holes towards the probe. More current is extracted on the $MACl$-treated sample up to -1250 pA, whereas it was only -175 pA for the untreated sample, see the current histograms in Figure 5.5c,f. This indicates that $MACl$ treatment helps more carriers to be collected under equal bias, thanks to the promotion of charge transfer and inhibition of recombination.[182, 183]



Figure 5.5: **Photoconductive AFM maps.** (a,d) dark and (b,e) illuminated cAFM maps with (c,f) current histograms of $FAPbI_3$ and $MACl$ treated $FAPbI_3$ samples consecutively, under -300 mV bias and 100 mW/cm^2 illumination acquired at $<$1% rH. Inset shows a zoomed in current range of $FAPbI_3$ sample.

$MACl$-enhanced defect passivation is also accompanied by improvement in the material's rH stability. Figure 5.6a-r shows topography, dark, and illuminated KPFM maps of $FAPbI_3$

and $MACl$ treated $FAPbI_3$ samples acquired at time stamps b, d, and f according to Figure 5.1. We did not observe any change in topography throughout the exposure to the stressors used in this experiment. For the KPFM measurements, Figure 5.6s shows that the $FAPbI_3$ material's average SPV has reduced from -110 mV to -29 mV with rH exposure, significantly losing its photoactivity. On the other hand, the $MACl$ treated $FAPbI_3$ material's average SPV has increased from -41 mV to -160 mV. This enhancement in the photogenerated charge redistribution is attributed to the passivation of the surface trap states.[182]



Figure 5.6: **KPFM maps of pristine and rH exposed $FAPbI_3$ and grain boundary statistics.** (a,d,e,j,m,p) Topography, (b,e,h,k,n,q) dark KPFM and (c,f,i,l,o,r) illuminated KPFM maps of pristine, 1h exposed and a total of 9h exposed $FAPbI_3$ and $MACl$ treated $FAPbI_3$ samples consecutively. The samples are exposed to 50% of rH in the AFM chamber and the measurements before and after exposure are acquired on the same location. (s) Grain boundary surface photovoltage (SPV) enhancement at 0, 1h, and 9h of 50% rH exposure, calculated from averaged values from 10 different GBs.

To complement the surface voltage analyses, we measured steady-state PL following a similar rH profile with the KPFM measurements (Figure 5.7a,b). The PL spectra acquired at the time stamps a-f are also shown in Figure 5.7c,d. At time stamp a, the $MACl$-treated sample shows higher PL intensity. PL enhancement with $MACl$ addition is also supported by existing literature.[177, 182, 190] After initial rH exposure (a through d), both samples show higher PL intensity compared to the intensity in a, as shown in Figure 5.7a. $MACl$ untreated sample shows a 68% increase in PL intensity after 1h of humidity exposure (compare points b and d), and the treated sample shows a 48% increase. Under inert environments like N_2, PL enhancement with humidity exposure is reported, attributed to moisture passivating the non-radiative recombination sites in the perovskites.[38] Mind that these have the opposite results from the measurements done in air, testing a combined effect of humidity and oxygen stressors, leading to a reduction in PL.[133]

$MACl$ untreated sample ends with a 40% loss (b to f) after a total of 9h of humidity exposure, on the other hand, the treated sample shows a 18% increase. In Figure 5.7b, the PL signal starts to decrease ∼3h after the second humidity ramp (between d and e) for the untreated sample. This shows that degradation is initiated. For the $MACl$ treated samples, we find that exposure to 50% rH for 9h improves the PL yield, delaying the degradation into non-photoactive products. As grain boundaries act as main pathways for the diffusion of water molecules[43], moisture can dissolve MA^+ from the lattice[44], and lower the activation energy for vacancy-mediated halide migration[192], leaving PbI_2 behind at the grain boundaries.[139] Therefore when the grain boundaries have excess Cl^- ions, these slow down the penetration of water molecules, and help boost the stability of

the perovskite against humidity.

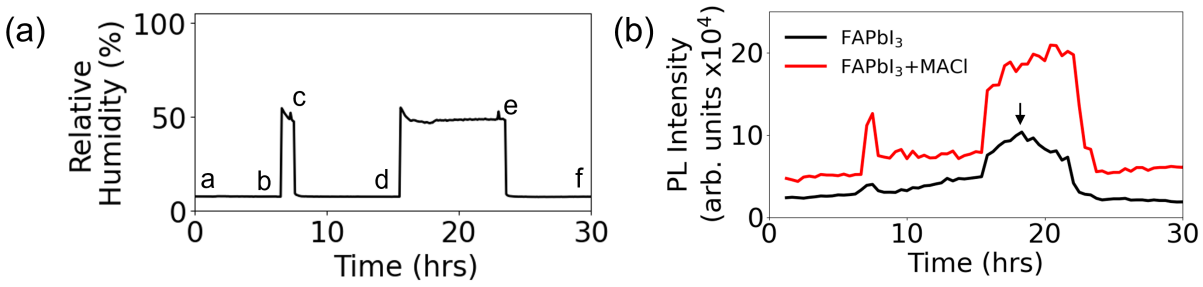


Figure 5.7: **Humidity-dependent photoluminescence characteristics.** (a) Humidity data acquired during PL measurements, (similar to the profile used for KPFM) with the intensity of PL spectra with respect to time. Time stamps labeled with a, b, c, d, e and f refer to where KPFM measurements were acquired for comparison. PL spectra of (b) $FAPbI_3$ and (c) $MACl$ treated $FAPbI_3$ acquired on these time stamps.

5.4 Conclusions

In summary, we mapped the transient surface voltage response of $FAPbI_3$ and $MACl$-treated $FAPbI_3$ perovskites, as a function of relative humidity under nitrogen. We found that $MACl$ helps with a more narrow size distribution of grains, accompanied by a more homogeneous distribution of surface voltage under illumination, and higher current extraction. Moreover, KPFM maps reveal that when exposed to 50% relative humidity under N_2, the addition of $MACl$ boosts the photogenerated charge redistribution, through trap states passivation.

Chapter 6: Conclusions and Outlook

In this thesis, I investigated optoelectronic processes in hybrid organic-inorganic perovskite (HOIP) thin films by combining *in situ* and *ex situ* microscopy experiments based on environmental KPFM and pcAFM. Specifically, I determined the effects of rH on the local electrical response of a series of HOIP materials, chosen due to their potential as cost-effective photovoltaic materials, with promising efficiencies.

First, we resolved the nanoscale surface photovoltage response of $Cs_{1/6}FA_{5/6}PbI_3$ HOIP upon exposure to moisture by performing *in situ*, rH-dependent KPFM measurements, capturing humidity-enhanced SPV. We discovered that the surface voltage is highly responsive to varying humidity. We found that the HOIP does not degrade readily upon exposure to a 9 h cycle with rH levels up to 65%. Before a degradation or morphological deterioration occurs, the reversible hydration of the top perovskite layers leads to rapid changes in the surface voltage distribution.

We attribute these effects to either ion migration, or to water-induced changes of the charge trap landscape at the hydrated semiconductor surface. Indeed, through chemical analyses, we found excess I^- on the perovskite surface, which tells us that I^- ions are

the migrated species. Whether this excess iodide is the origin of the observed enhanced photovoltage or a side product of slow perovskite degradation in wet air remains uncertain. Further studies are required to distinguish the ion migration from the charge trapping model.

Further, through *ex situ* rH exposure studies of $FAPbI_3$ and $MACl$ treated $FAPbI_3$ samples, we investigated the role of additives in surface photovoltage and humidity stabilization, after exposure to 50% rH for 1h and 9h. With KPFM measurements, we showed that the addition of $MACl$ additives can help improve the morphology by increasing the homogeneity of size distribution, in addition to increasing the homogeneity of the surface photovoltage. With correlative rH dependent KPFM and *in situ* PL measurements, we demonstrated that $MACl$ improves optoelectronic properties of $FAPbI_3$ perovskites through passivating defects at grain boundaries and boosts humidity stability. Our work reveals the role of $MACl$ additives in improving the voltage characteristics and stability of halide perovskites.

Dynamically deconvoluting the role of relative humidity and light on HOIP materials through nanoscale imaging, especially with advanced electrical methods such as KPFM, allows an understanding of the functional properties of materials such as charge carrier dynamics and ion migration, well beyond the conventional topography measurements. This technique can be applied to different compositions and the environmental stressors can be diversified. We anticipate that dynamic high-resolution microscopy will be the ground-breaker, revealing the instability behavior of conventional and emerging HOIP materials with precise control of the environmental conditions, *ex situ* or *in situ*, qualitatively and

quantitatively.

In the realm of perovskite photovoltaics, the greatest barrier for commercialization is the stability of materials under environmental stressors. Substantial work remains ahead for a holistic understanding of degradation mechanisms of HOIPs for optimization and commercial deployment, through uncovering the exact mechanism of interaction between the perovskite and water, and in real-life situations, a combination of multiple stressors. Nevertheless, functional imaging methods at the mesoscale present a pathway toward mapping the dynamical electrical response of materials under various environmental conditions and can be applied to additional HOIP families, including Pb-free perovskites. An exciting next step stemming from our work would be to implement ultrafast environmental KPFM measurements automated to perform compositional screening with different surface and bulk additives. We expect, that utilizing state-of-the-art technology, including robots during fabrication for better replicability of samples, machine learning for compositional screening, automated imaging, and faster image processing and registration through artificial intelligence tools will accelerate the process of achieving perovskite technologies with higher efficiency and stability.

Appendix: A Products of This Research

A.1 Awards and Honors

2. American Chemical Society Fall 2023 Division of Energy and Fuels Student Travel Award (Silver) 08/2023

1. Jeffery and Marsha Gibeling Materials Science and Engineering Fellowship 09/2019

A.2 Publications

7. **Deniz, E.**, Lee, D.K., Sutter-Fella, C., Leite, M.S. Chloride-based additives improve moisture stability of halide perovskites *(in preparation)*

6. **Deniz, E.**, Lyu, P., Dubey, M., Hering, A.R., Leite, M.S., et.al., Mesoscale water effects on surface response of CdTe solar cells *(in preparation)*

5. **Deniz, E.** and Lahoti, R., Kim, S., Duncan, M.A., Hidalgo, J., LaFollette, D., Correa-Baena, J.P., Leite, M.S. moisture-enhanced photovoltage response in hybrid perovskites via in-situ microscopy *(in preparation)*

4. Lyu, P., Matusalem, F., **Deniz, E.**, Rocha A.R., and Leite, M.S. In situ solid-state dewetting of Ag-Au-Pd alloy from macro- to nanoscale *(submitted)*

3. Wood, J.G., van Buuren, L., Guo, Z., **Deniz, E.**, Leite, M.S., Carpenter, A.C., Hunt,

C.E., van Benthem, K., Electrolytic etching of Ge substrates with H2O2, 2023 J. Electrochemical Society 170(10), 103503.

2. Palm, K. J., Gong, T., Shelden, C., **Deniz, E.**, Krayer, L. J., Leite, M. S., & Munday, J. N. Achieving scalable near-zero-index materials, 2022 Advanced Photonics Research, 3(9), 2200109.

1. Farinha, T. G., Gong, T., Lyu, P., **Deniz, E.**, Hoerauf, J. M., & Leite, M. S. (2021). Selective etching properties of Mg thin films and micro/nanostructures for dynamic photonics, Optical Materials Express, 11(5), 1555-1565.

A.3 Presentations

5. **Deniz, E.**, Leite, M. S. Functional imaging of perovskite materials via microscopy 2024 How Curious Graduate Research Series, UC Davis, Davis, CA (05/2024), talk.

4. **Deniz, E.**, Lahoti, R., Duncan, M.A., Kim, S., Hidalgo, J., LaFollette, D., Correa-Baena, J.P., Leite, M. S. Humidity-enhanced photovoltage in hybrid perovskites 2023 CHMS Research Symposium UC Davis, Davis, CA (09/2023), poster.

3. **Deniz, E.**, Lahoti, R., Duncan, M.A., Kim, S., Hidalgo, J., LaFollette, D., Correa-Baena, J.P., Leite, M. S. Humidity-enhanced photovoltage in hybrid perovskites, ACS Fall 2023, San Francisco, CA (08/2023), talk.

2. **Deniz, E.**, Leite, M. S. In Situ Microscopy Analysis of Humidity Response in Hybrid Perovskites. 2022 CHMS Research Symposium UC Davis, Davis, CA (09/2022), talk.

1. **Deniz, E.**, Fuller, E., Talin, A.A., Leite, M. S. Imaging Interfaces and Interphases in All-Solid-State Batteries at Nanoscale. MRS Fall 2023, Boston, MA (11/2021), talk.

Appendix: B Codes utilized

B.1 Drift correction

This python code applies drift correction on topography data through stack registration, then applies the necessary aligning on the voltage data (it is possible to do drift correction only on a stack of voltage data through using part of this code, however topography data often have more matching features making it easier for stack registration algorithm to work)

```
import numpy as np
from scipy.signal import fftconvolve
from scipy.ndimage import gaussian_filter

# Function to apply Gaussian filtering and normalize an image
def preprocess_image(image, sigma=1):
    filtered_image = gaussian_filter(image, sigma=sigma)
    normalized_image = (filtered_image - np.mean(filtered_image)) / np.std(
        filtered_image)
    return normalized_image
```

```
# Function to load data from a text file
def load_data(file_path):
    return np.loadtxt(file_path)


# Function to save data to a text file
def save_data(data, file_path):
    np.savetxt(file_path, data, delimiter='\t')


# Function to find the translational shift using FFT
def find_shift_fft(image_reference, image_to_align):
    correlation = fftconvolve(image_reference, image_to_align[::-1, ::-1], mode='
        same')
    max_index = np.unravel_index(np.argmax(correlation), correlation.shape)
    shift = np.array(max_index) - np.array(image_reference.shape) // 2
    return shift


# Function to apply the calculated shift to align images
def apply_shift(image, shift):
    return np.roll(np.roll(image, shift[0], axis=0), shift[1], axis=1)


# Function to trim edges of the aligned images to remove artifacts
def trim_edges(images, shift):
    y_min, x_min = np.max(np.abs(shift), axis=0)
    y_max, x_max = images[0].shape[0] - y_min, images[0].shape[1] - x_min
```

```
    return [img[y_min:y_max, x_min:x_max] for img in images]


# Define paths for topography and voltage data files, more can be added, make sure
    topographyfileX and voltagefileX are pairs from simultaneous data acquisition
topography_paths = ['topographyfile1.txt', ' topographyfile2.txt', ]
voltage_paths = ['voltagefile1.txt', ' voltagefile2.txt', ]


# Load, preprocess, and align topography images
topography_images = [preprocess_image(load_data(path)) for path in topography_paths
    ]
shifts = [find_shift_fft(topography_images[0], img) for img in topography_images
    [1:]]
aligned_topography_images = [topography_images[0]] + [
    apply_shift(topography_images[i+1], shift) for i, shift in enumerate(shifts)
]


# Load, preprocess, and align voltage images using the same shifts
voltage_images = [preprocess_image(load_data(path)) for path in voltage_paths]
aligned_voltage_images = [apply_shift(voltage_images[i], shifts[i-1] if i > 0 else
    (0,0))
                      for i in range(len(voltage_images))]
# Save the file according to the requirements
```

B.2 Watershed-based segmentation

Watershed-based segmentation is implemented with Python and Gwyddion software, following the methods and codes described in the references.[157, 158, 159, 161]

Bibliography

[1] "The Paris Agreement | UNFCCC,"

[2] "Solar and wind to lead growth of U.S. power generation for the next two years - U.S. Energy Information Administration (EIA),"

[3] T. Mai, D. Sandor, R. Wiser, and T. Schneider, "Renewable Electricity Futures Study: Executive Summary," p. 55.

[4] "Electric Power Annual," tech. rep., 2022.

[5] M. S. Chowdhury, K. S. Rahman, T. Chowdhury, N. Nuthammachot, K. Techato, M. Akhtaruzzaman, S. K. Tiong, K. Sopian, and N. Amin, "An overview of solar photovoltaic panels' end-of-life material recycling," *Energy Strategy Reviews*, vol. 27, p. 100431, Jan. 2020.

[6] G. Conibeer, "Third-generation photovoltaics," *Materials Today*, vol. 10, pp. 42–50, Nov. 2007.

[7] M. Giannouli, "Current Status of Emerging PV Technologies: A Comparative Study of Dye-Sensitized, Organic, and Perovskite Solar Cells," *International Journal of Photoenergy*, vol. 2021, pp. 1–19, May 2021.

[8] A. K. Jena, A. Kulkarni, and T. Miyasaka, "Halide Perovskite Photovoltaics: Background, Status, and Future Prospects," *Chemical Reviews*, vol. 119, pp. 3036–3103, Mar. 2019.

[9] "National Renewable Energy Laboratories. NREL Best Research-Cell Efficiencies.," 2022.

[10] A. Kojima, K. Teshima, Y. Shirai, and T. Miyasaka, "Organometal halide perovskites as visible-light sensitizers for photovoltaic cells," *Journal of the American Chemical Society*, vol. 131, pp. 6050–6051, May 2009.

[11] S. F. Hoefler, G. Trimmel, and T. Rath, "Progress on lead-free metal halide perovskites for photovoltaic applications: a review," *Monatshefte für Chemie - Chemical Monthly*, vol. 148, pp. 795–826, May 2017.

[12] G. Kieslich, S. Sun, and A. K. Cheetham, "An extended Tolerance Factor approach for organic–inorganic perovskites," *Chemical Science*, vol. 6, no. 6, pp. 3430–3433, 2015.

[13] M. Abdelsamie, J. Xu, K. Bruening, C. J. Tassone, H. Steinrück, and M. F. Toney, "Impact of Processing on Structural and Compositional Evolution in Mixed Metal Halide Perovskites during Film Formation," *Advanced Functional Materials*, vol. 30, p. 2001752, Sept. 2020.

[14] G. F. Novikov and M. V. Gapanovich, "Third-generation Cu-In-Ga-(S, Se)-based solar inverters," p. 19.

[15] M. Kim, G.-H. Kim, K. S. Oh, Y. Jo, H. Yoon, K.-H. Kim, H. Lee, J. Y. Kim, and D. S. Kim, "High-Temperature–Short-Time Annealing Process for High-Performance Large-Area Perovskite Solar Cells," *ACS Nano*, vol. 11, pp. 6057–6064, June 2017.

[16] Q. Cao, S. Yang, Q. Gao, L. Lei, Y. Yu, J. Shao, and Y. Liu, "Fast and Controllable Crystallization of Perovskite Films by Microwave Irradiation Process," *ACS Applied Materials & Interfaces*, vol. 8, pp. 7854–7861, Mar. 2016.

[17] S. You, S. Bi, J. Huang, Q. Jia, Y. Yuan, Y. Xia, Z. Xiao, Z. Sun, J. Liu, S. Sun, and Z. Zhao, "Additive-Enhanced Crystallization of Solution Process for Planar Perovskite Solar Cells with Efficiency Exceeding 19 %," *Chemistry - A European Journal*, vol. 23, pp. 18140–18145, Dec. 2017.

[18] S. Mabrouk, B. Bahrami, A. Gurung, K. M. Reza, N. Adhikari, A. Dubey, R. Pathak, S. Yang, and Q. Qiao, "Higher efficiency perovskite solar cells using additives of LiI, LiTFSI and BMImI in the PbI 2 precursor," *Sustainable Energy & Fuels*, vol. 1, no. 10, pp. 2162–2171, 2017.

[19] T. Salim, S. Sun, Y. Abe, A. Krishna, A. C. Grimsdale, and Y. M. Lam, "Perovskite-based solar cells: impact of morphology and device architecture on device performance," *Journal of Materials Chemistry A*, vol. 3, no. 17, pp. 8943–8969, 2015.

[20] Y. Li, L. Ji, R. Liu, C. Zhang, C. H. Mak, X. Zou, H.-H. Shen, S.-Y. Leu, and H.-Y. Hsu, "A review on morphology engineering for highly efficient and stable hybrid perovskite solar cells," *Journal of Materials Chemistry A*, vol. 6, no. 27, pp. 12842–12875, 2018.

[21] M. Srivastava, J. M. Howard, T. Gong, M. Rebello Sousa Dias, and M. S. Leite, "Machine learning roadmap for perovskite photovoltaics," *The Journal of Physical Chemistry Letters*, vol. 12, no. 32, pp. 7866–7877, 2021.

[22] G. Richardson, S. E. J. O'Kane, R. G. Niemann, T. A. Peltola, J. M. Foster, P. J. Cameron, and A. B. Walker, "Can slow-moving ions explain hysteresis in the current–voltage curves of perovskite solar cells?," *Energy & Environmental Science*, vol. 9, no. 4, pp. 1476–1485, 2016.

[23] S. Ravishankar, O. Almora, C. Echeverría-Arrondo, E. Ghahremanirad, C. Aranda, A. Guerrero, F. Fabregat-Santiago, A. Zaban, G. Garcia-Belmonte, and J. Bisquert,

"Surface Polarization Model for the Dynamic Hysteresis of Perovskite Solar Cells," *The Journal of Physical Chemistry Letters*, vol. 8, pp. 915–921, Mar. 2017.

[24] Y. Zhang, M. Liu, G. E. Eperon, T. C. Leijtens, D. McMeekin, M. Saliba, W. Zhang, M. de Bastiani, A. Petrozza, L. M. Herz, M. B. Johnston, H. Lin, and H. J. Snaith, "Charge selective contacts, mobile ions and anomalous hysteresis in organic–inorganic perovskite solar cells," *Materials Horizons*, vol. 2, no. 3, pp. 315–322, 2015.

[25] T. Zhang, H. Chen, Y. Bai, S. Xiao, L. Zhu, C. Hu, Q. Xue, and S. Yang, "Understanding the relationship between ion migration and the anomalous hysteresis in high-efficiency perovskite solar cells: A fresh perspective from halide substitution," *Nano Energy*, vol. 26, pp. 620–630, Aug. 2016.

[26] Z. Zhou, S. Pang, Z. Liu, H. Xu, and G. Cui, "Interface engineering for high-performance perovskite hybrid solar cells," *Journal of Materials Chemistry A*, vol. 3, no. 38, pp. 19205–19217, 2015.

[27] A.-N. Cho and N.-G. Park, "Impact of interfacial layers in perovskite solar cells," *ChemSusChem*, vol. 10, pp. 3687–3704, Oct. 2017.

[28] Y. C. Kim, N. J. Jeon, J. H. Noh, W. S. Yang, J. Seo, J. S. Yun, A. Ho-Baillie, S. Huang, M. A. Green, J. Seidel, T. K. Ahn, and S. I. Seok, "Beneficial Effects of PbI 2 Incorporated in Organo-Lead Halide Perovskite Solar Cells," *Advanced Energy Materials*, vol. 6, p. 1502104, Feb. 2016.

[29] Y. Reyna, M. Salado, S. Kazim, A. Pérez-Tomas, S. Ahmad, and M. Lira-Cantu, "Performance and stability of mixed FAPbI3(0.85)MAPbBr3(0.15) halide perovskite solar cells under outdoor conditions and the effect of low light irradiation," *Nano Energy*, vol. 30, pp. 570–579, Dec. 2016.

[30] J. F. Galisteo-López, M. E. Calvo, and H. Míguez, "The Complex Interplay of Lead Halide Perovskites with Their Surroundings," *Advanced Optical Materials*, vol. 9, p. 2100133, Sept. 2021.

[31] R. L. Milot, G. E. Eperon, H. J. Snaith, M. B. Johnston, and L. M. Herz, "Temperature-Dependent Charge-Carrier Dynamics in CH 3 NH 3 PbI 3 Perovskite Thin Films," *Advanced Functional Materials*, vol. 25, pp. 6218–6227, Oct. 2015.

[32] P. Holzhey, P. Yadav, S.-H. Turren-Cruz, A. Ummadisingu, M. Grätzel, A. Hagfeldt, and M. Saliba, "A chain is as strong as its weakest link – Stability study of MAPbI3 under light and temperature," *Materials Today*, vol. 29, pp. 10–19, Oct. 2019.

[33] R. E. Beal, N. Z. Hagström, J. Barrier, A. Gold-Parker, R. Prasanna, K. A. Bush, D. Passarello, L. T. Schelhas, K. Brüning, C. J. Tassone, H.-G. Steinrück, M. D. McGehee, M. F. Toney, and A. F. Nogueira, "Structural Origins of Light-Induced Phase Segregation in Organic-Inorganic Halide Perovskite Photovoltaic Materials," *Matter*, vol. 2, pp. 207–219, Jan. 2020.

[34] F. Matsumoto, S. M. Vorpahl, J. Q. Banks, E. Sengupta, and D. S. Ginger, "Photodecomposition and Morphology Evolution of Organometal Halide Perovskite Solar Cells," *The Journal of Physical Chemistry C*, vol. 119, pp. 20810–20816, Sept. 2015.

[35] J. Barbé, V. Kumar, M. J. Newman, H. K. H. Lee, S. M. Jain, H. Chen, C. Charbonneau, C. Rodenburg, and W. C. Tsoi, "Dark electrical bias effects on moisture-induced degradation in inverted lead halide perovskite solar cells measured by using advanced chemical probes," *Sustainable Energy & Fuels*, vol. 2, no. 4, pp. 905–914, 2018.

[36] S. T. Birkhold, J. T. Precht, H. Liu, R. Giridharagopal, G. E. Eperon, L. Schmidt-Mende, X. Li, and D. S. Ginger, "Interplay of mobile ions and injected carriers creates recombination centers in metal halide perovskites under bias," *ACS Energy Letters*, vol. 3, pp. 1279–1286, June 2018.

[37] P. Raval, R. M. Kennard, E. S. Vasileiadou, C. J. Dahlman, I. Spanopoulos, M. L. Chabinyc, M. Kanatzidis, and G. N. Manjunatha Reddy, "Understanding Instability in Formamidinium Lead Halide Perovskites: Kinetics of Transformative Reactions at Grain and Subgrain Boundaries," *ACS Energy Letters*, vol. 7, pp. 1534–1543, Apr. 2022.

[38] J. M. Howard, E. M. Tennyson, S. Barik, R. Szostak, E. Waks, M. F. Toney, A. F. Nogueira, B. R. A. Neves, and M. S. Leite, "Humidity-Induced Photoluminescence Hysteresis in Variable Cs/Br Ratio Hybrid Perovskites," *The Journal of Physical Chemistry Letters*, vol. 9, pp. 3463–3469, June 2018.

[39] N. Aristidou, I. Sanchez-Molina, T. Chotchuangchutchaval, M. Brown, L. Martinez, T. Rath, and S. A. Haque, "The Role of Oxygen in the Degradation of Methylammonium Lead Trihalide Perovskite Photoactive Layers," *Angewandte Chemie*, vol. 127, pp. 8326–8330, July 2015.

[40] M. Anaya, J. F. Galisteo-López, M. E. Calvo, J. P. Espinós, and H. Míguez, "Origin of light-induced photophysical effects in organic metal halide perovskites in the presence of oxygen," *The Journal of Physical Chemistry Letters*, vol. 9, pp. 3891–3896, July 2018.

[41] Y. An, J. Hidalgo, C. A. R. Perini, A.-F. Castro-Méndez, J. N. Vagott, K. Bairley, S. Wang, X. Li, and J.-P. Correa-Baena, "Structural Stability of Formamidinium- and Cesium-Based Halide Perovskites," *ACS Energy Letters*, vol. 6, pp. 1942–1969, May 2021.

[42] G. Grancini, C. Roldán-Carmona, I. Zimmermann, E. Mosconi, X. Lee, D. Martineau, S. Narbey, F. Oswald, F. De Angelis, M. Graetzel, and M. K. Nazeeruddin, "One-Year stable perovskite solar cells by 2D/3D interface engineering," *Nature Communications*, vol. 8, p. 15684, Aug. 2017.

[43] A. M. A. Leguy, Y. Hu, M. Campoy-Quiles, M. I. Alonso, O. J. Weber, P. Azarhoosh, M. van Schilfgaarde, M. T. Weller, T. Bein, J. Nelson, P. Docampo, and P. R. F.

Barnes, "Reversible Hydration of CH 3 NH 3 PbI 3 in Films, Single Crystals, and Solar Cells," *Chemistry of Materials*, vol. 27, pp. 3397–3407, May 2015.

[44] G. E. Eperon, S. N. Habisreutinger, T. Leijtens, B. J. Bruijnaers, J. J. van Franeker, D. W. deQuilettes, S. Pathak, R. J. Sutton, G. Grancini, D. S. Ginger, R. A. J. Janssen, A. Petrozza, and H. J. Snaith, "The Importance of Moisture in Hybrid Lead Halide Perovskite Thin Film Fabrication," *ACS Nano*, vol. 9, pp. 9380–9393, Sept. 2015.

[45] K. K. Bass, R. E. McAnally, S. Zhou, P. I. Djurovich, M. E. Thompson, and B. C. Melot, "Influence of moisture on the preparation, crystal structure, and photophysical properties of organohalide perovskites," *Chem. Commun.*, vol. 50, no. 99, pp. 15819–15822, 2014.

[46] J. Lee and N. Park, "Chemical Approaches for Stabilizing Perovskite Solar Cells," *Advanced Energy Materials*, vol. 10, p. 1903249, Jan. 2020.

[47] S. Dastidar, D. A. Egger, L. Z. Tan, S. B. Cromer, A. D. Dillon, S. Liu, L. Kronik, A. M. Rappe, and A. T. Fafarman, "High Chloride Doping Levels Stabilize the Perovskite Phase of Cesium Lead Iodide," *Nano Letters*, vol. 16, pp. 3563–3570, June 2016.

[48] C. C. Stoumpos, C. D. Malliakas, and M. G. Kanatzidis, "Semiconducting Tin and Lead Iodide Perovskites with Organic Cations: Phase Transitions, High Mobilities, and Near-Infrared Photoluminescent Properties," *Inorganic Chemistry*, vol. 52, pp. 9019–9038, Aug. 2013.

[49] J.-W. Lee, D.-H. Kim, H.-S. Kim, S.-W. Seo, S. M. Cho, and N.-G. Park, "Formamidinium and Cesium Hybridization for Photo- and Moisture-Stable Perovskite Solar Cell," *Advanced Energy Materials*, vol. 5, p. 1501310, Oct. 2015.

[50] T. Liu, Y. Zong, Y. Zhou, M. Yang, Z. Li, O. S. Game, K. Zhu, R. Zhu, Q. Gong, and N. P. Padture, "High-performance formamidinium-based perovskite solar cells via microstructure-mediated δ to α phase transformation," *Chemistry of Materials*, vol. 29, pp. 3246–3250, Apr. 2017.

[51] P. E. Marchezi, E. M. Therézio, R. Szostak, H. C. Loureiro, K. Bruening, A. Gold-Parker, M. A. Melo, C. J. Tassone, H. C. N. Tolentino, M. F. Toney, and A. F. Nogueira, "Degradation mechanisms in mixed-cation and mixed-halide Cs x FA 1-x Pb(Br y I 1-y) 3 perovskite films under ambient conditions," *Journal of Materials Chemistry A*, vol. 8, no. 18, pp. 9302–9312, 2020.

[52] M. Saliba, T. Matsui, J.-Y. Seo, K. Domanski, J.-P. Correa-Baena, M. K. Nazeeruddin, S. M. Zakeeruddin, W. Tress, A. Abate, A. Hagfeldt, and M. Grätzel, "Cesium-containing triple cation perovskite solar cells: improved stability, reproducibility and high efficiency," *Energy & Environmental Science*, vol. 9, no. 6, pp. 1989–1997, 2016.

[53] S. Ašmontas, A. Čerškus, J. Gradauskas, A. Grigucevičienė, R. Juškėnas, K. Leinartas, A. Lučun, K. Petrauskas, A. Selskis, A. Sužiedėlis, and E. Širmulis, "Impact of Cesium Concentration on Optoelectronic Properties of Metal Halide Perovskites," *Materials*, vol. 15, p. 1936, Mar. 2022.

[54] Z. Li, M. Yang, J.-S. Park, S.-H. Wei, J. J. Berry, and K. Zhu, "Stabilizing Perovskite Structures by Tuning Tolerance Factor: Formation of Formamidinium and Cesium Lead Iodide Solid-State Alloys," *Chemistry of Materials*, vol. 28, pp. 284–292, Jan. 2016.

[55] Y. An, C. A. R. Perini, J. Hidalgo, A.-F. Castro-Méndez, J. N. Vagott, R. Li, W. A. Saidi, S. Wang, X. Li, and J.-P. Correa-Baena, "Identifying high-performance and durable methylammonium-free lead halide perovskites via high-throughput synthesis and characterization," *Energy & Environmental Science*, vol. 14, no. 12, pp. 6638–6654, 2021.

[56] J. Hieulle, C. Stecker, R. Ohmann, L. K. Ono, and Y. Qi, "Scanning Probe Microscopy Applied to Organic-Inorganic Halide Perovskite Materials and Solar Cells," *Small Methods*, vol. 2, p. 1700295, Jan. 2018.

[57] E. M. Tennyson, C. Gong, and M. S. Leite, "Imaging Energy Harvesting and Storage Systems at the Nanoscale," *ACS Energy Letters*, vol. 2, pp. 2761–2777, Dec. 2017.

[58] Y. Kobayashi, Y. Miyake, F. Ishiwari, S. Ishiwata, and A. Saeki, "Machine learning of atomic force microscopy images of organic solar cells," *RSC Advances*, vol. 13, no. 22, pp. 15107–15113, 2023.

[59] S. W. Schmitt, R. K. Vasudevan, M. Seifert, A. Y. Borisevich, V. Deshpande, S. V. Kalinin, and C. Dubourdieu, "Sub-10 nm Probing of Ferroelectricity in Heterogeneous Materials by Machine Learning Enabled Contact Kelvin Probe Force Microscopy," *ACS Applied Electronic Materials*, vol. 3, pp. 4409–4417, Oct. 2021.

[60] T. Dittrich and S. Fengler, *Surface Photovoltage Analysis of Photoactive Materials*. Feb. 2020.

[61] S. Kavadiya, A. Onno, C. Boyd, Z. Yu, M. McGehee, and Z. C. Holman, "Surface Photovoltage Measurement of Perovskite Solar Cells to Screen Carrier Selective Contacts," in *2020 47th IEEE Photovoltaic Specialists Conference (PVSC)*, (Calgary, AB, Canada), pp. 1439–1440, June 2020.

[62] D. A. Bonnell, S. V. Kalinin, D. A. Bonnell, and S. V. Kalinin, eds., *Scanning probe microscopy for energy research*. World scientific series in nanoscience and nanotechnology, 2013.

[63] Y. Kutes, Y. Zhou, J. L. Bosse, J. Steffes, N. P. Padture, and B. D. Huey, "Mapping the Photoresponse of CH 3 NH 3 PbI 3 Hybrid Perovskite Thin Films at the Nanoscale," *Nano Letters*, vol. 16, pp. 3434–3441, June 2016.

[64] J. L. Garrett, E. M. Tennyson, M. Hu, J. Huang, J. N. Munday, and M. S. Leite, "Real-Time Nanoscale Open-Circuit Voltage Dynamics of Perovskite Solar Cells," *Nano Letters*, vol. 17, pp. 2554–2560, Apr. 2017.

[65] J. M. Howard, R. Lahoti, and M. S. Leite, "Imaging Metal Halide Perovskites Material and Properties at the Nanoscale," *Advanced Energy Materials*, vol. 10, p. 1903161, July 2020.

[66] R. Kerr, T. J. Macdonald, A. J. Tanner, J. Yu, J. A. Davies, H. H. Fielding, and G. Thornton, "Zero Threshold for Water Adsorption on MAPbBr3," *Small*, vol. 19, no. 40, p. 2301014, 2023.

[67] M. Vrućinić, C. Matthiesen, A. Sadhanala, G. Divitini, S. Cacovich, S. E. Dutton, C. Ducati, M. Atatüre, H. Snaith, R. H. Friend, H. Sirringhaus, and F. Deschler, "Local Versus Long-Range Diffusion Effects of Photoexcited States on Radiative Recombination in Organic-Inorganic Lead Halide Perovskites," *Advanced Science*, vol. 2, p. 1500136, Sept. 2015.

[68] C. S. Pathak, B.-J. Chang, and S. Song, "Review on scanning probe microscopy analysis for perovskite materials and solar cells," *Dyes and Pigments*, vol. 218, p. 111469, Oct. 2023.

[69] F. Zhang, H. Zhang, and J. Song, "Abnormal Boost in Photovoltaic Performance and Stability of Perovskite Solar Cells in High Humidity Test Environment," *The Journal of Physical Chemistry C*, p. acs.jpcc.3c04371, Oct. 2023.

[70] J.-Y. Ma, J. Ding, H.-J. Yan, D. Wang, and J.-S. Hu, "Temperature-Dependent Local Electrical Properties of Organic–Inorganic Halide Perovskites: In Situ KPFM and c-AFM Investigation," *ACS Applied Materials & Interfaces*, vol. 11, pp. 21627–21633, June 2019.

[71] L. Collins, M. Ahmadi, T. Wu, B. Hu, S. V. Kalinin, and S. Jesse, "Breaking the Time Barrier in Kelvin Probe Force Microscopy: Fast Free Force Reconstruction Using the G-Mode Platform," *ACS Nano*, vol. 11, pp. 8717–8729, Sept. 2017.

[72] R. Chen, F. Fan, T. Dittrich, and C. Li, "Imaging photogenerated charge carriers on surfaces and interfaces of photocatalysts with surface photovoltage microscopy," *Chemical Society Reviews*, vol. 47, no. 22, pp. 8238–8262, 2018.

[73] J. S. Yun, J. Kim, T. Young, R. J. Patterson, D. Kim, J. Seidel, S. Lim, M. A. Green, S. Huang, and A. Ho-Baillie, "Humidity-induced degradation via grain boundaries of hc(nh2)2pbi3 planar perovskite solar cells," *Advanced Functional Materials*, vol. 28, p. 1705363, Mar. 2018.

[74] W. Melitz, J. Shen, A. C. Kummel, and S. Lee, "Kelvin probe force microscopy and its application," *Surface Science Reports*, vol. 66, pp. 1–27, Jan. 2011.

[75] M. Nonnenmacher, M. P. O'Boyle, and H. K. Wickramasinghe, "Kelvin probe force microscopy," p. 4.

[76] R. T. . Tung, "The physics and chemistry of the Schottky barrier height," *Applied Physics Reviews*, vol. 1, p. 011304, Jan. 2014.

[77] Y. Almadori, D. Moerman, J. L. Martinez, P. Leclère, and B. Grévin, "Multimodal noncontact atomic force microscopy and Kelvin probe force microscopy investigations of organolead tribromide perovskite single crystals," *Beilstein Journal of Nanotechnology*, vol. 9, pp. 1695–1704, June 2018.

[78] D. He, X. Xu, Z. Liang, Y. Niu, Y. Sun, T. Gavin, P. Falaras, and L. Hu, "Defect passivation and humidity protection for perovskite solar cells enabled by 1-dodecanethiol," *Journal of Materials Chemistry C*, vol. 9, no. 30, pp. 9584–9591, 2021.

[79] W. H. Brattain, "Evidence for Surface States on Semiconductors from Change in Contact Potential on Illumination," *Physical Review*, vol. 72, pp. 345–345, Aug. 1947.

[80] W. H. Brattain and J. Bardeen, "Surface properties of germanium," *The Bell System Technical Journal*, vol. 32, pp. 1–41, Jan. 1953.

[81] C. G. B. Garrett and W. H. Brattain, "Physical Theory of Semiconductor Surfaces," *Physical Review*, vol. 99, pp. 376–387, July 1955.

[82] A. Bojar, D. Regaldo, J. Alvarez, D. Alamarguy, V. Donchev, S. Georgiev, P. Schulz, and J.-P. Kleider, "Surface photovoltage characterisation of metal halide perovskite on crystalline silicon using kelvin probe force microscopy and metal-insulator-semiconductor configuration," *EPJ Photovoltaics*, vol. 13, p. 18, 2022.

[83] J. S. Yun, A. Ho-Baillie, S. Huang, S. H. Woo, Y. Heo, J. Seidel, F. Huang, Y.-B. Cheng, and M. A. Green, "Benefit of grain boundaries in organic-inorganic halide planar perovskite solar cells," *The Journal of Physical Chemistry Letters*, vol. 6, pp. 875–880, Mar. 2015.

[84] L. Collins, M. Ahmadi, J. Qin, Y. Liu, O. S. Ovchinnikova, B. Hu, J. Stephen, and S. V. Kalinin, "Time resolved surface photovoltage measurements using a big data capture approach to kpfm," *Nanotechnology*, vol. 29, p. 445703, 2018.

[85] L. Kronik, "Surface photovoltage phenomena: theory, experiment, and applications," *Surface Science Reports*, vol. 37, pp. 1–206, 1999.

[86] L. Barnea-Nehoshtan, S. Kirmayer, E. Edri, G. Hodes, and D. Cahen, "Surface Photovoltage Spectroscopy Study of Organo-Lead Perovskite Solar Cells," *The Journal of Physical Chemistry Letters*, vol. 5, pp. 2408–2413, July 2014.

[87] R. M. Doughty, F. A. Chowdhury, Z. Mi, and F. E. Osterloh, "Surface photovoltage spectroscopy observes junctions and carrier separation in gallium nitride nanowire arrays for overall water-splitting," *The Journal of Chemical Physics*, vol. 153, p. 144707, Oct. 2020.

[88] J. Zhao and F. E. Osterloh, "Photochemical Charge Separation in Nanocrystal Photocatalyst Films: Insights from Surface Photovoltage Spectroscopy," *The Journal of Physical Chemistry Letters*, vol. 5, pp. 782–786, Mar. 2014.

[89] Z. Kang, H. Si, M. Shi, C. Xu, W. Fan, S. Ma, A. Kausar, Q. Liao, Z. Zhang, and Y. Zhang, "Kelvin probe force microscopy for perovskite solar cells," *Science China Materials*, vol. 62, pp. 776–789, June 2019.

[90] Q. Hu, D. Alikin, B. Slautin, A. Turygin, X. Liu, P. Li, Y. Zhang, D. Lin, K. Song, Y. Zhuang, Z. Xu, P. Zelenovskiy, V. Y. Shur, and X. Wei, "Nanoscale investigation on electric field induced ferroelectric phase transitions in the rhombohedral PMN-PT single crystal," *JOURNAL OF ALLOYS AND COMPOUNDS*, vol. 953, p. 170118, Aug. 2023.

[91] Y. Gao, W. Nie, Q. Zhu, X. Wang, S. Wang, F. Fan, and C. Li, "The Polarization Effect in Surface-Plasmon-Induced Photocatalysis on Au/TiO 2 Nanoparticles," *Angewandte Chemie International Edition*, vol. 59, pp. 18218–18223, Oct. 2020.

[92] H. Hoppe, T. Glatzel, M. Niggemann, A. Hinsch, M. C. Lux-Steiner, and N. S. Sariciftci, "Kelvin Probe Force Microscopy Study on Conjugated Polymer/Fullerene Bulk Heterojunction Organic Solar Cells," *Nano Letters*, vol. 5, pp. 269–274, Feb. 2005.

[93] W. Dou, F. Qi, Y. Li, F. Wei, Q. Hu, Z. Yao, J. Wang, L. Zhang, and Z. Tang, "Charge-biased nanofibrous membranes with uniform charge distribution and hemocompatibility for enhanced selective adsorption of endotoxin from plasma," *JOURNAL OF MEMBRANE SCIENCE*, vol. 666, p. 121134, Jan. 2023.

[94] B. Bahrami, A. H. Chowdhury, A. Gurung, S. Mabrouk, K. M. Reza, S. I. Rahman, R. Pathak, and Q. Qiao, "Nanoscale spatial mapping of charge carrier dynamics in perovskite solar cells," *Nano Today*, vol. 33, p. 100874, Aug. 2020.

[95] J.-J. Li, J.-Y. Ma, Q.-Q. Ge, J.-S. Hu, D. Wang, and L.-J. Wan, "Microscopic Investigation of Grain Boundaries in Organolead Halide Perovskite Solar Cells," *ACS Applied Materials & Interfaces*, vol. 7, pp. 28518–28523, Dec. 2015.

[96] B. Yang, C. C. Brown, J. Huang, L. Collins, X. Sang, R. R. Unocic, S. Jesse, S. V. Kalinin, A. Belianinov, J. Jakowski, D. B. Geohegan, B. G. Sumpter, K. Xiao, and O. S. Ovchinnikova, "Enhancing Ion Migration in Grain Boundaries of Hybrid Organic–Inorganic Perovskites by Chlorine," *Advanced Functional Materials*, vol. 27, p. 1700749, July 2017.

[97] J.-W. Lee, S.-G. Kim, J.-M. Yang, Y. Yang, and N.-G. Park, "Verification and mitigation of ion migration in perovskite solar cells," *APL Materials*, vol. 7, p. 041111, Apr. 2019.

[98] J. Mizusaki, K. Arai, and K. Fueki, "Ionic conduction of the perovskite-type halides," *Solid State Ionics*, vol. 11, pp. 203–211, Nov. 1983.

[99] T. Yang, G. Gregori, N. Pellet, M. Grätzel, and J. Maier, "The Significance of Ion Conduction in a Hybrid Organic–Inorganic Lead-Iodide-Based Perovskite Photosensitizer," *Angewandte Chemie*, vol. 127, pp. 8016–8021, June 2015.

[100] H. J. Snaith, A. Abate, J. M. Ball, G. E. Eperon, T. Leijtens, N. K. Noel, S. D. Stranks, J. T.-W. Wang, K. Wojciechowski, and W. Zhang, "Anomalous hysteresis in perovskite solar cells," *The Journal of Physical Chemistry Letters*, vol. 5, pp. 1511–1515, May 2014.

[101] E. L. Unger, E. T. Hoke, C. D. Bailie, W. H. Nguyen, A. R. Bowring, T. Heumüller, M. G. Christoforo, and M. D. McGehee, "Hysteresis and transient behavior in current–voltage measurements of hybrid-perovskite absorber solar cells," *Energy Environ. Sci.*, vol. 7, no. 11, pp. 3690–3698, 2014.

[102] G. Xia, B. Huang, Y. Zhang, X. Zhao, C. Wang, C. Jia, J. Zhao, W. Chen, and J. Li, "Nanoscale Insights into Photovoltaic Hysteresis in Triple-Cation Mixed-Halide Perovskite: Resolving the Role of Polarization and Ionic Migration," *Advanced Materials*, vol. 31, no. 36, p. 1902870, 2019.

[103] D. W. deQuilettes, W. Zhang, V. M. Burlakov, D. J. Graham, T. Leijtens, A. Osherov, V. Bulović, H. J. Snaith, D. S. Ginger, and S. D. Stranks, "Photo-induced halide redistribution in organic–inorganic perovskite films," *Nature Communications*, vol. 7, p. 11683, May 2016.

[104] T. Zhang, X. Meng, Y. Bai, S. Xiao, C. Hu, Y. Yang, H. Chen, and S. Yang, "Profiling the organic cation-dependent degradation of organolead halide perovskite solar cells," *Journal of Materials Chemistry A*, vol. 5, no. 3, pp. 1103–1111, 2017.

[105] J. M. Azpiroz, E. Mosconi, J. Bisquert, and F. De Angelis, "Defect migration in methylammonium lead iodide and its role in perovskite solar cell operation," *Energy & Environmental Science*, vol. 8, no. 7, pp. 2118–2127, 2015.

[106] T. Zhang, S. H. Cheung, X. Meng, L. Zhu, Y. Bai, C. H. Y. Ho, S. Xiao, Q. Xue, S. K. So, and S. Yang, "Pinning Down the Anomalous Light Soaking Effect toward High-Performance and Fast-Response Perovskite Solar Cells: The Ion-Migration-Induced Charge Accumulation," *The Journal of Physical Chemistry Letters*, vol. 8, pp. 5069–5076, Oct. 2017.

[107] C. Zhao, B. Chen, X. Qiao, L. Luan, K. Lu, and B. Hu, "Revealing Underlying Processes Involved in Light Soaking Effects and Hysteresis Phenomena in Perovskite Solar Cells," *Advanced Energy Materials*, vol. 5, p. 1500279, July 2015.

[108] T. Z. a. C. H. a. S. Yang, "Ion Migration: A "Double-Edged Sword" for Halide-Perovskite-Based Electronic Devices | EndNote Click."

[109] S. Draguta, S. Thakur, Y. V. Morozov, Y. Wang, J. S. Manser, P. V. Kamat, and M. Kuno, "Spatially Non-uniform Trap State Densities in Solution-Processed Hybrid Perovskite Thin Films," *The Journal of Physical Chemistry Letters*, vol. 7, pp. 715–721, Feb. 2016.

[110] S. D. Stranks, V. M. Burlakov, T. Leijtens, J. M. Ball, A. Goriely, and H. J. Snaith, "Recombination Kinetics in Organic-Inorganic Perovskites: Excitons, Free Charge, and Subgap States," *Physical Review Applied*, vol. 2, p. 034007, Sept. 2014.

[111] A. Walsh, D. O. Scanlon, S. Chen, X. G. Gong, and S. Wei, "Self-Regulation Mechanism for Charged Point Defects in Hybrid Halide Perovskites," *Angewandte Chemie*, vol. 127, pp. 1811–1814, Feb. 2015.

[112] Y. W. Woo, Z. Li, Y.-K. Jung, J.-S. Park, and A. Walsh, "Inhomogeneous Defect Distribution in Mixed-Polytype Metal Halide Perovskites," *ACS Energy Letters*, vol. 8, pp. 356–360, Jan. 2023.

[113] C. Eames, J. M. Frost, P. R. F. Barnes, B. C. O'Regan, A. Walsh, and M. S. Islam, "Ionic transport in hybrid lead iodide perovskite solar cells," *Nature Communications*, vol. 6, p. 7497, June 2015.

[114] F. Lou, S. Yuan, X. Wang, H.-Y. Wang, Y. Wang, Y. Qin, X.-C. Ai, and J.-P. Zhang, "Distinguishing the migration time scale of ion species in perovskite solar cells," *Chemical Physics Letters*, vol. 796, p. 139570, June 2022.

[115] L. A. Muscarella, E. M. Hutter, F. Wittmann, Y. W. Woo, Y.-K. Jung, L. McGovern, J. Versluis, A. Walsh, H. J. Bakker, and B. Ehrler, "Lattice Compression Increases the Activation Barrier for Phase Segregation in Mixed-Halide Perovskites," *ACS Energy Letters*, vol. 5, pp. 3152–3158, Oct. 2020.

[116] Z. Xiao, Y. Yuan, Y. Shao, Q. Wang, Q. Dong, C. Bi, P. Sharma, A. Gruverman, and J. Huang, "Giant switchable photovoltaic effect in organometal trihalide perovskite devices," *Nature Materials*, vol. 14, pp. 193–198, Feb. 2015. ion migration.

[117] H. Lu, A. Krishna, S. M. Zakeeruddin, M. Grätzel, and A. Hagfeldt, "Compositional and Interface Engineering of Organic-Inorganic Lead Halide Perovskite Solar Cells," *iScience*, vol. 23, p. 101359, Aug. 2020.

[118] N. J. Jeon, J. H. Noh, W. S. Yang, Y. C. Kim, S. Ryu, J. Seo, and S. I. Seok, "Compositional engineering of perovskite materials for high-performance solar cells," *Nature*, vol. 517, pp. 476–480, Jan. 2015.

[119] M. Saliba, T. Matsui, K. Domanski, J.-Y. Seo, A. Ummadisingu, S. M. Zakeeruddin, J.-P. Correa-Baena, W. R. Tress, A. Abate, A. Hagfeldt, and M. Grätzel, "Incorporation of rubidium cations into perovskite solar cells improves photovoltaic performance," *Science (New York, N.Y.)*, vol. 354, pp. 206–209, Oct. 2016.

[120] J. H. Noh, S. H. Im, J. H. Heo, T. N. Mandal, and S. I. Seok, "Chemical Management for Colorful, Efficient, and Stable Inorganic–Organic Hybrid Nanostructured Solar Cells," *Nano Letters*, vol. 13, pp. 1764–1769, Apr. 2013.

[121] C. Li, G. Chen, W. Wang, J. Zhang, L. Wu, X. Hao, and L. Feng, "Grain boundary passivation by CdCl2 treatment in CdTe solar cells revealed by Kelvin probe force microscopy," *Journal of Materials Science: Materials in Electronics*, vol. 29, pp. 20718–20725, Dec. 2018.

[122] Y. Shao, Y. Fang, T. Li, Q. Wang, Q. Dong, Y. Deng, Y. Yuan, H. Wei, M. Wang, A. Gruverman, J. Shield, and J. Huang, "Grain boundary dominated ion migration in polycrystalline organic–inorganic halide perovskite films," *Energy & Environmental Science*, vol. 9, no. 5, pp. 1752–1759, 2016.

[123] Y. Liu, S. Yuan, H. Zheng, M. Wu, S. Zhang, J. Lan, W. Li, and J. Fan, "Structurally Dimensional Engineering in Perovskite Photovoltaics," *Advanced Energy Materials*, vol. 13, p. 2300188, June 2023.

[124] J.-F. Liao, H.-S. Rao, B.-X. Chen, D.-B. Kuang, and C.-Y. Su, "Dimension engineering on cesium lead iodide for efficient and stable perovskite solar cells," *Journal of Materials Chemistry A*, vol. 5, pp. 2066–2072, Feb. 2017.

[125] S. Heo, G. Seo, K. T. Cho, Y. Lee, S. Paek, S. Kim, M. Seol, S. H. Kim, D.-J. Yun, K. Kim, J. Park, J. Lee, L. Lechner, T. Rodgers, J. W. Chung, J.-S. Kim, D. Lee, S.-H. Choi, and M. K. Nazeeruddin, "Dimensionally Engineered Perovskite Heterostructure for Photovoltaic and Optoelectronic Applications," *Advanced Energy Materials*, vol. 9, p. 1902470, Dec. 2019.

[126] J. Kim, S.-H. Lee, J. H. Lee, and K.-H. Hong, "The Role of Intrinsic Defects in Methylammonium Lead Iodide Perovskite," *The Journal of Physical Chemistry Letters*, vol. 5, pp. 1312–1317, Apr. 2014.

[127] W.-J. Yin, T. Shi, and Y. Yan, "Unusual defect physics in CH3NH3PbI3 perovskite solar cell absorber," *Applied Physics Letters*, vol. 104, p. 063903, Feb. 2014.

[128] J. L. Garrett and J. N. Munday, "Fast, high-resolution surface potential measurements in air with heterodyne Kelvin probe force microscopy," *Nanotechnology*, vol. 27, p. 245705, June 2016.

[129] J. S. Yun, J. Seidel, J. Kim, A. M. Soufiani, S. Huang, J. Lau, N. J. Jeon, S. I. Seok, M. A. Green, and A. Ho-Baillie, "Critical Role of Grain Boundaries for Ion Migration in Formamidinium and Methylammonium Lead Halide Perovskite Solar Cells," *Adv. Energy Mater.*, p. 8, 2016.

[130] V. W. Bergmann, S. A. L. Weber, F. Javier Ramos, M. K. Nazeeruddin, M. Grätzel, D. Li, A. L. Domanski, I. Lieberwirth, S. Ahmad, and R. Berger, "Real-space observation of unbalanced charge distribution inside a perovskite-sensitized solar cell," *Nature Communications*, vol. 5, p. 5001, Dec. 2014.

[131] H. Sugimura, Y. Ishida, K. Hayashi, O. Takai, and N. Nakagiri, "Potential shielding by the surface water layer in Kelvin probe force microscopy," *Applied Physics Letters*, vol. 80, pp. 1459–1461, Feb. 2002.

[132] W. Yao, Q. Ling, Q. Dai, S. Fang, C. Yang, L. Huang, X. Liu, H. Zhang, J. Zhang, Y. Zhu, and Z. Hu, "In Situ Microscopic Observation of Humidity-Induced Degradation in All-Inorganic Perovskite Films," *ACS Applied Energy Materials*, p. acsaem.2c00576, June 2022.

[133] K.-L. Huang, Y.-H. Chang, P.-Y. Lin, K.-W. Hsu, D. E. Beck, and S. Hsieh, "Humidity Effects on Pure and Doped All-Inorganic Perovskite Thin Films Analyzed by Scanning Probe Microscopy," *The Journal of Physical Chemistry C*, vol. 126, pp. 13441–13448, Aug. 2022.

[134] C. Liu, W. Kong, W. Li, H. Chen, D. Li, W. Wang, B. Xu, C. Cheng, and A. K. Y. Jen, "Enhanced stability and photovoltage for inverted perovskite solar cells via precursor engineering," *Journal of Materials Chemistry A*, vol. 7, no. 26, pp. 15880–15886, 2019.

[135] M. F. Mohamad Noh, N. A. Arzaee, I. N. Nawas Mumthas, N. A. Mohamed, S. N. F. Mohd Nasir, J. Safaei, A. R. B. M. Yusoff, M. K. Nazeeruddin, and M. A. Mat Teridi, "High-humidity processed perovskite solar cells," *Journal of Materials Chemistry A*, vol. 8, no. 21, pp. 10481–10518, 2020.

[136] R. Wang, M. Mujahid, Y. Duan, Z.-K. Wang, J. Xue, and Y. Yang, "A Review of Perovskites Solar Cell Stability," *Advanced Functional Materials*, vol. 29, no. 47, p. 1808843, 2019.

[137] J. Jiménez-López and E. Palomares, "Interfacial recombination kinetics in aged perovskite solar cells measured using transient photovoltage techniques," *Nanoscale*, vol. 11, no. 42, pp. 20024–20029, 2019.

[138] S.-J. Kim, Y. Kim, R. K. Chitumalla, G. Ham, T.-D. Nguyen, J. Jang, H. Cha, J. Milić, J.-H. Yum, K. Sivula, and J.-Y. Seo, "Interfacial engineering through lead binding using crown ethers in perovskite solar cells," *Journal of Energy Chemistry*, vol. 92, pp. 263–270, May 2024.

[139] M. N. F. Hoque, R. He, J. Warzywoda, and Z. Fan, "Effects of Moisture-Based Grain Boundary Passivation on Cell Performance and Ionic Migration in Organic–Inorganic Halide Perovskite Solar Cells," *ACS Applied Materials & Interfaces*, vol. 10, pp. 30322–30329, Sept. 2018.

[140] B. P. Kore, M. Jamshidi, and J. M. Gardner, "The impact of moisture on the stability and degradation of perovskites in solar cells," *Materials Advances*, pp. 2200–2217, 2024.

[141] Z. Li, C. Xiao, Y. Yang, S. P. Harvey, D. H. Kim, J. A. Christians, M. Yang, P. Schulz, S. U. Nanayakkara, C.-S. Jiang, J. M. Luther, J. J. Berry, M. C. Beard, M. M. Al-Jassim, and K. Zhu, "Extrinsic ion migration in perovskite solar cells," *Energy & Environmental Science*, vol. 10, no. 5, pp. 1234–1242, 2017.

[142] C. C. Ahia and E. L. Meyer, "Advances in the Use of Atomic Force Microscopy as a Diagnostic Tool for Solar Cells Characterization: From Material Design to Device Applications," *physica status solidi (a)*, p. 2300293, Dec. 2023.

[143] J. Y. Park, S. Maier, B. Hendriksen, and M. Salmeron, "Sensing current and forces with SPM," *Materials Today*, vol. 13, pp. 38–45, Oct. 2010.

[144] H. Si, S. Zhang, S. Ma, Z. Xiong, A. Kausar, Q. Liao, Z. Zhang, A. Sattar, Z. Kang, and Y. Zhang, "Emerging Conductive Atomic Force Microscopy for Metal Halide Perovskite Materials and Solar Cells," *Advanced Energy Materials*, vol. 10, no. 10, p. 1903922, 2020.

[145] S. Y. Leblebici, L. Leppert, Y. Li, S. E. Reyes-Lillo, S. Wickenburg, E. Wong, J. Lee, M. Melli, D. Ziegler, D. K. Angell, D. F. Ogletree, P. Ashby, F. M. Toma, J. B. Neaton, I. D. Sharp, and A. Weber-Bargioni, "Facet-dependent photovoltaic efficiency variations in single grains of hybrid halide perovskite," *Nature Energy*, vol. 1, p. 16093, July 2016.

[146] B. Moores, F. Hane, L. Eng, and Z. Leonenko, "Kelvin probe force microscopy in application to biomolecular films: Frequency modulation, amplitude modulation, and lift mode," *Ultramicroscopy*, vol. 110, pp. 708–711, May 2010.

[147] G. H. Enevoldsen, "Scanning Probe Microscopy Studies of a Metal Oxide Surface,"

[148] C. C. Ahia and E. L. Meyer, "Advances in the Use of Atomic Force Microscopy as a Diagnostic Tool for Solar Cells Characterization: From Material Design to Device Applications," *physica status solidi (a)*, vol. 221, p. 2300293, Feb. 2024.

[149] B. Lägel, I. D. Baikie, and U. Petermann, "A novel detection system for defects and chemical contamination in semiconductors based upon the Scanning Kelvin Probe," *Surface Science*, vol. 433-435, pp. 622–626, Aug. 1999.

[150] L. Collins, J. I. Kilpatrick, S. V. Kalinin, and B. J. Rodriguez, "Towards nanoscale electrical measurements in liquid by advanced KPFM techniques: a review," *Reports on Progress in Physics*, vol. 81, p. 086101, Aug. 2018.

[151] T. Wang, C. Ma, Y. Chen, J. Chu, and W. Huang, "Effects of temperature and humidity on atomic force microscopy dimensional measurement," *Microscopy Research and Technique*, vol. 78, pp. 562–568, July 2015.

[152] C. Yang, P. Du, Z. Dai, H. Li, X. Yang, and Q. Chen, "Effects of Illumination Direction on the Surface Potential of CH 3 NH 3 PbI 3 Perovskite Films Probed by Kelvin Probe Force Microscopy," *ACS Applied Materials & Interfaces*, vol. 11, pp. 14044–14050, Apr. 2019.

[153] G. Alosaimi, S. J. Shin, R. L. Chin, J. H. Kim, J. S. Yun, and J. Seidel, "Probing Charge Carrier Properties and Ion Migration Dynamics of Indoor Halide Perovskite PV Devices Using Top- and Bottom-Illumination SPM Studies," *Advanced Energy Materials*, vol. 11, no. 37, p. 2101739, 2021.

[154] S. Biswas and H. Kim, "Solar Cells for Indoor Applications: Progress and Development," *Polymers*, vol. 12, p. 1338, June 2020.

[155] "Reference Air Mass 1.5 Spectra."

[156] M. Sonka, V. Hlavac, and R. Boyle, *Image processing, analysis, and machine vision*. Chapman & Hall computing series, 1st ed ed., 1993.

[157] L. Vincent and P. Soille, "Watersheds in digital spaces: an efficient algorithm based on immersion simulations," *IEEE Transactions on Pattern Analysis and Machine Intelligence*, vol. 13, pp. 583–598, June 1991.

[158] P. Klapetek, I. Ohlídal, A. Montaigne-Ramil, A. Bonanni, D. Stifter, and H. Sitter, "Atomic Force Microscopy Characterization of ZnTe Epitaxial Thin Films," *Japanese Journal of Applied Physics*, vol. 42, pp. 4706–4709, July 2003.

[159] The scikit-image team, "Watershed segmentation,"

[160] D. o. N. Czech Metrology Institute *Statistical Analysis - Chapter 4. Data Processing and Analysis*.

[161] D. o. N. Czech Metrology Institute *Grain Analysis - Chapter 4. Data Processing and Analysis*.

[162] V. W. Bergmann, Y. Guo, H. Tanaka, I. M. Hermes, D. Li, A. Klasen, S. A. Bretschneider, E. Nakamura, R. Berger, and S. A. L. Weber, "Local time-dependent charging in a perovskite solar cell," *ACS Applied Materials & Interfaces*, vol. 8, pp. 19402–19409, 2016.

[163] B. C. O'Regan, P. R. F. Barnes, X. Li, C. Law, E. Palomares, and J. M. Marin-Beloqui, "Optoelectronic studies of methylammonium lead iodide perovskite solar cells with mesoporous tio2: Separation of electronic and chemical charge storage, understanding two recombination lifetimes, and the evolution of band offsets during j–v hysteresis," *Journal of the American Chemical Society*, vol. 137, pp. 5087–5099, 2015.

[164] Y. Liu, A. V. Ievlev, N. Borodinov, M. Lorenz, K. Xiao, M. Ahmadi, B. Hu, S. V. Kalinin, and O. S. Ovchinnikova, "Direct observation of photoinduced ion migration in lead halide perovskites," *Advanced Functional Materials*, vol. 31, p. 2008777, 2021.

[165] D. W. de Quilettes, S. M. Vorpahl, S. D. Stranks, H. Nagaoka, G. E. Eperon, M. E. Ziffer, H. J. Snaith, and D. S. Ginger, "Impact of microstructure on local carrier lifetime in perovskite solar cells," *Science*, vol. 348, pp. 683–686, May 2015.

[166] J. Guo, B. Wang, D. Lu, T. Wang, T. Liu, R. Wang, X. Dong, T. Zhou, N. Zheng, Q. Fu, Z. Xie, X. Wan, G. Xing, Y. Chen, and Y. Liu, "Ultralong carrier lifetime exceeding 20 in lead halide perovskite film enable efficient solar cells," *Advanced Materials*, vol. 35, p. 2212126, 2023.

[167] L. Zhang, M. Zhou, Z. Zhang, J. Yuan, B. Li, W. Wen, and J. Tian, "Ultra-long photoluminescence lifetime in an inorganic halide perovskite thin film," *Journal of Materials Chemistry A*, vol. 7, pp. 22229–22234, 2019.

[168] E. M. Tennyson, B. Roose, J. L. Garrett, C. Gong, J. N. Munday, A. Abate, and M. S. Leite, "Cesium-Incorporated Triple Cation Perovskites Deliver Fully Reversible and Stable Nanoscale Voltage Response," *ACS Nano*, p. acsnano.8b07295, Jan. 2019.

[169] I. S. Zhidkov, A. I. Poteryaev, A. Kukharenko, L. D. Finkelstein, S. O. Cholakh, A. F. Akbulatov, P. A. Troshin, C. C. Cheh, and E. Z. Kurmaev, "Xps evidence of degradation mechanism in hybrid halide perovskites," *Journal of Physics: Condensed Matter*, vol. 32, p. 095501, 2020.

[170] S. Maniyarasu, B. F. Spencer, H. Mo, A. S. Walton, A. G. Thomas, and W. R. Flavell, "Surface stability of ionic-liquid-passivated mixed-cation perovskite probed with in situ photoelectron spectroscopy," *Journal of Materials Chemistry A*, vol. 10, pp. 18206–18217, 2022.

[171] F. Baumann, S. R. Raga, and M. Lira-Cantú, "Monitoring the stability and degradation mechanisms of perovskite solar cells by in situ and operando characterization," *2023*, vol. 1, p. 011501, 2023.

[172] K. Park, S. Tan, T. Kodalle, D. Lee, M. Abdelsamie, J. Park, J. Lee, S. Jung, J. H. Ko, N. Park, C. M. Sutter-Fella, Y. Yang, and J. Lee, "Atmospheric Humidity Underlies Irreproducibility of Formamidinium Lead Iodide Perovskites," *Advanced Materials*, p. 2307265, Dec. 2023.

[173] F. Zhang and K. Zhu, "Additive Engineering for Efficient and Stable Perovskite Solar Cells," *Advanced Energy Materials*, vol. 10, p. 1902579, Apr. 2020.

[174] M. M. Byranvand and M. Saliba, "Defect Passivation of Perovskite Films for Highly Efficient and Stable Solar Cells," *Solar RRL*, vol. 5, p. 2100295, Aug. 2021.

[175] E. Pineda De La O, N. Alhazmi, S. J. Ebbens, and A. D. F. Dunbar, "Influence of Additives on the In Situ Crystallization Dynamics of Methyl Ammonium Lead Halide Perovskites," *ACS Applied Energy Materials*, vol. 4, pp. 1398–1409, Feb. 2021.

[176] Y. Zhao and K. Zhu, "CH3NH3Cl-Assisted One-Step Solution Growth of CH3NH3PbI3: Structure, Charge-Carrier Dynamics, and Photovoltaic Properties of Perovskite Solar Cells," *The Journal of Physical Chemistry C*, vol. 118, pp. 9412–9418, May 2014.

[177] M. Kim, G.-H. Kim, T. K. Lee, I. W. Choi, H. W. Choi, Y. Jo, Y. J. Yoon, J. W. Kim, J. Lee, D. Huh, H. Lee, S. K. Kwak, J. Y. Kim, and D. S. Kim, "Kim, minjin, et al. "methylammonium chloride induces intermediate phase stabilization for efficient perovskite solar cells," *Joule*, vol. 3, pp. 2179–2192, Sept. 2019.

[178] T. S. Sherkar, C. Momblona, L. Gil-Escrig, J. Ávila, M. Sessolo, H. J. Bolink, and L. J. A. Koster, "Recombination in Perovskite Solar Cells: Significance of Grain Boundaries, Interface Traps, and Defect Ions," *ACS Energy Letters*, vol. 2, pp. 1214–1222, May 2017.

[179] D. Kim, K. Higgins, and M. Ahmadi, "Navigating grain boundaries in perovskite solar cells," *Matter*, vol. 4, pp. 1442–1445, May 2021.

[180] F. Ji, S. Pang, L. Zhang, Y. Zong, G. Cui, N. P. Padture, and Y. Zhou, "Simultaneous Evolution of Uniaxially Oriented Grains and Ultralow-Density Grain-Boundary Network in CH3NH3PbI3 Perovskite Thin Films Mediated by Precursor Phase Metastability," *ACS Energy Letters*, vol. 2, pp. 2727–2733, Dec. 2017.

[181] Q. Chen, H. Zhou, Y. Fang, A. Z. Stieg, T.-B. Song, H.-H. Wang, X. Xu, Y. Liu, S. Lu, J. You, P. Sun, J. McKay, M. S. Goorsky, and Y. Yang, "The optoelectronic role of chlorine in CH3NH3PbI3(Cl)-based perovskite solar cells," *Nature Communications*, vol. 6, p. 7269, June 2015.

[182] Y. Guo, S. Yuan, D. Zhu, M. Yu, H.-Y. Wang, J. Lin, Y. Wang, Y. Qin, J.-P. Zhang, and X.-C. Ai, "Influence of the macl additive on grain boundaries, trap-state properties, and charge dynamics in perovskite solar cells," *Physical Chemistry Chemical Physics*, vol. 23, pp. 6162–6170, Mar. 2021.

[183] V. Larini, M. Degani, G. Pica, C. Ding, Z. Andaji-Garmaroudi, F. Faini, S. D. Stranks, C.-Q. Ma, and G. Grancini, "From Bulk to Surface Passivation: Double Role of Chlorine-Doping for Boosting Efficiency of FAPbI3-rich Perovskite Solar Cells," *Solar RRL*, vol. 6, no. 8, p. 2200038, 2022.

[184] T. A. Berhe, W.-N. Su, C.-H. Chen, C.-J. Pan, J.-H. Cheng, H.-M. Chen, M.-C. Tsai, L.-Y. Chen, A. A. Dubale, and B.-J. Hwang, "Organometal halide perovskite solar cells: degradation and stability," *Energy & Environmental Science*, vol. 9, pp. 323–356, Feb. 2016.

[185] H. Yu, F. Wang, F. Xie, W. Li, J. Chen, and N. Zhao, "The Role of Chlorine in the Formation Process of "CH3NH3PbI3-xClx" Perovskite," *Advanced Functional Materials*, vol. 24, no. 45, pp. 7102–7108, 2014.

[186] R. K. Misra, S. Aharon, B. Li, D. Mogilyansky, I. Visoly-Fisher, L. Etgar, and E. A. Katz, "Temperature- and Component-Dependent Degradation of Perovskite Photovoltaic Materials under Concentrated Sunlight," *The Journal of Physical Chemistry Letters*, vol. 6, pp. 326–330, Feb. 2015.

[187] Y. Tidhar, E. Edri, H. Weissman, D. Zohar, G. Hodes, D. Cahen, B. Rybtchinski, and S. Kirmayer, "Crystallization of Methyl Ammonium Lead Halide Perovskites: Implications for Photovoltaic Applications," *Journal of the American Chemical Society*, vol. 136, pp. 13249–13256, Sept. 2014.

[188] M. Antoniadou, E. Siranidi, N. Vaenas, A. G. Kontos, E. Stathatos, and P. Falaras, "Photovoltaic Performance and Stability of CH3NH3PbI3–x Cl x Perovskites," *Journal of Surfaces and Interfaces of Materials*, vol. 2, pp. 323–327, Dec. 2014.

[189] G. Li, T. Zhang, N. Guo, F. Xu, X. Qian, and Y. Zhao, "Ion-exchange-induced 2d–3d conversion of hma1-xfaxpbi3cl perovskite into a high-quality ma1-xfaxpbi3 perovskite," *Angewandte Chemie International Edition*, vol. 55, pp. 13460–13464, 2016.

[190] H. Wang and J. Zhang, "Methylammonium chloride additive in lead iodide optimizing the crystallization process for efficient perovskite solar cells," *International Journal of Photoenergy*, vol. 2022, p. 5288400, 2022.

[191] J. Xue, R. Wang, and Y. Yang, "The surface of halide perovskites from nano to bulk," *Nature Reviews Materials*, vol. 5, pp. 809–827, Nov. 2020.

[192] U.-G. Jong, C.-J. Yu, G.-C. Ri, A. P. McMahon, N. M. Harrison, P. R. Barnes, and A. Walsh, "Influence of water intercalation and hydration on chemical decomposition and ion transport in methylammonium lead halide perovskites," *Journal of Materials Chemistry A*, pp. 1067–1074, 2018.